

Cyclic Deformation Behavior of a Rare-Earth Containing Extruded Magnesium Alloy: Effect of Heat Treatment

F.A. MIRZA, D.L. CHEN, D.J. LI, and X.Q. ZENG

The present study was aimed at evaluating strain-controlled cyclic deformation behavior of a rare-earth (RE) element containing Mg-10Gd-3Y-0.5Zr (GW103K) alloy in different states (as-extruded, peak-aged (T5), and solution-treated and peak-aged (T6)). The addition of RE elements led to an effective grain refinement and weak texture in the as-extruded alloy. While heat treatment resulted in a grain growth modestly in the T5 state and significantly in the T6 state, a high density of nano-sized and bamboo-leaf/plate-shaped β' (Mg₇(Gd,Y)) precipitates was observed to distribute uniformly in the α -Mg matrix. The yield strength and ultimate tensile strength, as well as the maximum and minimum peak stresses during cyclic deformation in the T5 and T6 states were significantly higher than those in the as-extruded state. Unlike RE-free extruded Mg alloys, symmetrical hysteresis loops in tension and compression and cyclic stabilization were present in the GW103K alloy in different states. The fatigue life of this alloy in the three conditions, which could be well described by the Coffin–Manson law and Basquin's equation, was equivalent within the experimental scatter and was longer than that of RE-free extruded Mg alloys. This was predominantly attributed to the presence of the relatively weak texture and the suppression of twinning activities stemming from the fine grain sizes and especially RE-containing β' precipitates. Fatigue crack was observed to initiate from the specimen surface in all the three alloy states and the initiation site contained some cleavage-like facets after T6 heat treatment. Crack propagation was characterized mainly by the characteristic fatigue striations.

DOI: 10.1007/s11661-014-2687-1

© The Minerals, Metals & Materials Society and ASM International 2014

I. INTRODUCTION

DUE to the tremendous environmental concerns and escalating global energy demand encountered by the transportation industry in recent years, lightweighting of vehicles is being deemed as a prime design tool for improving the fuel economy and reducing anthropogenic climate-changing, environment-damaging, costly, and human death-causing* emissions.^[1–6] It is today even referred

to as the “storm” of lightweighting—a revolution in materials, processes, and business models, which is brewing on the horizon of the automotive and aerospace industry. To fabricate lighterweight vehicles, advanced high-strength steels, aluminum alloys, magnesium (Mg) alloys, and polymers are being used in the aerospace and automotive sectors, but substantial reductions could be further achieved by employing ultra-lightweight Mg alloys due to their low density, high strength-to-weight ratio, and superior damping capacity.^[1,2,7] There are currently intensive studies in the development of wrought Mg alloys with high strength, high corrosion resistance, and superior formability for structural applications.^[8,9] Despite the potential of substantial reductions in weight, most wrought Mg alloys exhibited unusual mechanical properties, *e.g.*, tension–compression yield asymmetry, limited ductility, and pronounced directional anisotropy arising from the presence of strong crystallographic texture related to their hexagonal close-packed (HCP) structure with a limited number of slip systems activated during extrusion or rolling processes.^[10–15] Indeed, for the vehicle components subjected to dynamic cyclic loading, such mechanical anisotropy and tension–compression yield asymmetry could lead to irreversibility of cyclic deformation which may have an unfavorable influence on the material performance.^[15]

These problems could be tackled through texture modification. One appealing approach of achieving this goal is *via* alloy composition adjustment, *e.g.*, addition of rare-earth (RE) elements into Mg alloys.^[15–30] These RE-Mg alloys possess quite random initial crystallographic texture which leads to improved ductility and

*According to Science News entitled “Air pollution kills 7 million people a year” on March 25, 2014 at <http://news.sciencemag.org/signal-noise/2014/03/air-pollution-kills-7-million-people-year>: “Air pollution is not just harming Earth; it is hurting us, too. Startling new numbers released by the World Health Organization today reveal that one in eight deaths are a result of exposure to air pollution. The data reveal a strong link between the tiny particles that we breathe into our lungs and the illnesses they can lead to, including stroke, heart attack, lung cancer, and chronic obstructive pulmonary disease.”

F.A. MIRZA, Ph.D. Student, and D.L. CHEN, Professor and Ryerson Research Chair, are with the Department of Mechanical and Industrial Engineering, Ryerson University, 350 Victoria Street, Toronto, ON M5B 2K3, Canada. Contact e-mail: dchen@ryerson.ca D.J. LI, Lecturer, and X.Q. ZENG, Professor, are with The State Key Laboratory of Metal Matrix Composites, School of Materials Science and Engineering, Shanghai Jiao Tong University, 800 Dongchuan Road, Shanghai 200240, P.R. China.

Manuscript submitted October 28, 2013.

Article published online December 4, 2014

strength at both room and elevated temperatures *via* solid solution strengthening and precipitation strengthening.^[31,32] It was reported that an RE element alternates the bonding energy between the Mg atom and the RE atom, thus increasing the possibility of non-basal slip and inhibiting the basal slip and {1012} twinning.^[32] In other words, RE elements such as Gd, Nd, Ce, and La can work as effective texture modifiers for Mg alloys, and they are able to produce the so-called “RE texture component” even at low alloying levels.^[18–20,23,26,27,33] Recent studies reported that due to certain RE concentrations and extrusion parameters there was a shift in the orientation peak of the extrusion textures in the RE-containing alloys from $\langle 10-10 \rangle$ to new positions of $\langle 11-21 \rangle$, $\langle 11-22 \rangle$ or $\langle 20-21 \rangle$ parallel to extrusion direction, which were termed as “RE texture component”.^[19,20,33] The components were well oriented for basal slip when tested in the appropriate orientation (where it is difficult to deform, resulting in high flow stresses, and modest work hardening^[34]), which results in a considerable gain of ductility and a reduction of the tension–compression asymmetry present in the conventional wrought Mg alloys.

Although these alterations in the tension–compression yield asymmetry due to the RE elements additions are being gradually enlightened, the potential advantage of such extruded RE-Mg alloys as structural components under dynamic cyclic loading condition has not yet been well appreciated. Most of the earlier studies were conducted mainly on the high cyclic fatigue properties of the RE-Mg alloys.^[15,35–41] Studies on the strain-controlled low-cycle fatigue behavior of RE-containing Mg alloys remain quite scarce to date.^[17,24,32,40–47] For example, Wang *et al.*^[32] studied the low-cycle fatigue behavior of extruded Mg-8.0Gd-3.0Y-0.5Zr (GW83) alloy under fully reversed strain-controlled tension–compression loading along the extrusion direction. Wu *et al.*^[42] investigated the strain-controlled low-cycle fatigue properties of a Mg-10Gd-2.0Y-0.46Zr alloy at 573 K (300 °C). To the authors’ knowledge, no systematic studies have been conducted to understand the effect of heat treatment conditions on the low cyclic fatigue behavior of RE-containing Mg alloys in the open literature. It has not been clearly illuminated how the cyclic deformation and low-cycle fatigue resistance change due to heat treatment, whether the heat-treated RE-Mg alloy exhibits cyclic hardening or softening, and what is the effect of the heat treatment on the tensile-compressive yield symmetry. Thus, an understanding about the effect of heat treatment on the cyclic deformation characteristics of RE-containing Mg alloys is necessary. The present study was aimed at exploring the cyclic deformation behavior of an extruded Mg-10Gd-3Y-0.5Zr (GW103K) alloy subjected to varying heat treatment procedures.

II. MATERIAL AND EXPERIMENTAL PROCEDURE

The material selected in the present study was a recently developed extruded Mg-10Gd-3Y-0.5Zr alloy, with an actual composition of 10.0 Gd, 2.7 Y, and 0.4 Zr (in

wt pct). The extrusion was performed at a temperature of 673 K (400 °C) with an extrusion ratio of 9:1 at an extrusion ram speed of 3 mm/s and a die angle of 60 deg. The entire process of heating and extrusion was completed within about 10 minutes, and the extruded bars were then water quenched. After extrusion, the extruded bars were subjected to two types of heat treatment: (1) direct peak-aging at 498 K (225 °C) for 16 hours (T5 heat treatment), and (2) solution at 773 K (500 °C) for 2 hours, then water cooling, followed by isothermally aging at 498 K (225 °C) for 16 hours in an oil bath furnace (T6 heat treatment). Microstructural examinations were performed using an optical microscope (OM) equipped with Clemex quantitative image analysis software, scanning electron microscope (SEM) JSM-6380LV equipped with Oxford energy dispersive X-ray spectroscopy (EDS) system and three-dimensional (3D) surface/fractographic analysis capacity, and transmission electron microscope (TEM, JEM-2100) operated at 200 kV. Standard metallographic sample preparation techniques were used with an etchant based on an acetic picral solution containing 4.2 g picric acid, 10 mL acetic acid, 10 mL H₂O, and 70 mL ethanol. The average grain size was measured *via* a linear intercept method. The texture was determined by measuring incomplete pole figures between $\Psi = 0$ to 75 deg in the back reflection mode using a PANalytical X’Pert PRO X-ray diffractometer (XRD) with Cu K_α radiation at 45 kV and 40 mA and analyzed using MTEX software. Defocusing due to the rotation of XRD sample holder was corrected using experimentally determined data obtained from the diffraction of Mg powders received from Magnesium Elektron. Sub-sized fatigue samples were machined with the loading axis parallel to the extrusion direction (ED). The samples had a gage length of 25 mm (or a parallel length of 32 mm) and a width of 6 mm. The thickness of the samples was 6 mm as well. The gage section of fatigue samples was ground progressively along the loading direction with emery papers up to a grit number of 600 to remove the machining marks and to achieve a consistent surface.

Strain-controlled, pull–push type fatigue tests were conducted using a computerized Instron 8801 fatigue testing system *via* a fast track low cycle fatigue (LCF) program at a constant strain rate of $1 \times 10^{-2} \text{ s}^{-1}$ and room temperature of 298 K (25 °C). The tests were carried out in a strain control mode according to ASTM E606 standard. Triangular strain waveform was applied during the tests. Low-cycle fatigue tests were performed at total strain amplitudes of 0.2, 0.4, 0.6, 0.8, 1.0, and 1.2 pct, and at least two samples were tested at each level of the strain amplitudes. The strain-controlled tests at lower strain amplitude levels were continued up to 10,000 cycles, then the tests were changed to load control at a frequency of 50 Hz using sine waveform. For the sake of comparison, some samples of RE-free extruded AM30 Mg alloy (with a composition of 3.4 wt pct Al, 0.33 wt pct Mn, 0.16 wt pct Zn, 0.0026 wt pct Fe, 0.0006 wt pct Ni, 0.0008 wt pct Cu, and balance Mg) were also tested. The fracture surfaces of fatigued specimens were examined *via* SEM to identify fatigue crack initiation sites and propagation characteristics. The residual twins in the region near the fracture surface were observed as well.

III. RESULTS

A. Microstructure and Crystallographic Texture

Figure 1 shows typical optical micrographs and SEM back-scattered electron images of GW103K alloy in different states (as-extruded, T5, and T6). It is seen from Figure 1(a) that uniform equiaxed grains with an average grain size of about $12\ \mu\text{m}$ were obtained in as-extruded sample due to the occurrence of dynamic recrystallization (DRX) in the hot extrusion process at $673\ \text{K}$ ($400\ ^\circ\text{C}$).^[24] The grain size of as-extruded sample

was fairly small in comparison with the common extruded Mg alloys, such as AZ31 and AM30,^[9–14] and the smaller grain size was due to the role of added RE elements and zirconium where Zr mainly restricted the grain growth.^[48] Figure 1(b) shows a typical SEM back-scattered electron image of as-extruded sample where several RE containing particles can be seen. By means of EDS point analysis, the content at points A, B, and C of Figure 1(b) was estimated to be 57.8 pct Mg-17.5 pct Y-22.5 pct Gd-2.2 pct Zr, 79.3 pct Mg-5.2 pct Y-15.0 pct Gd-0.5 pct Zr, and 84.9 pct

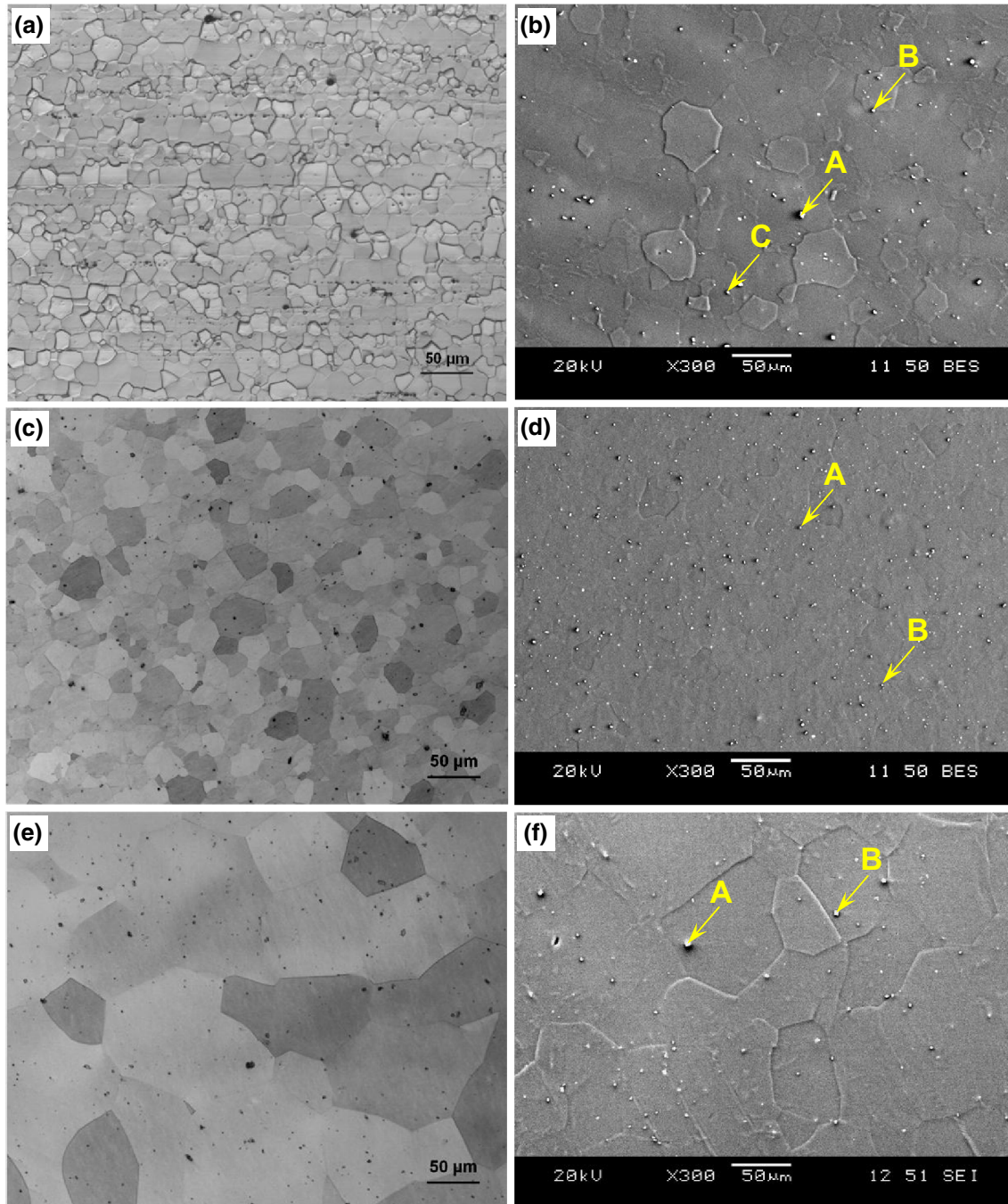


Fig. 1—Microstructures (left optical micrographs and right SEM back-scattered electron images) of the GW103K alloy in the (a)^[24] and (b) as-extruded, (c) and (d) T5, and (e) and (f) T6 states.

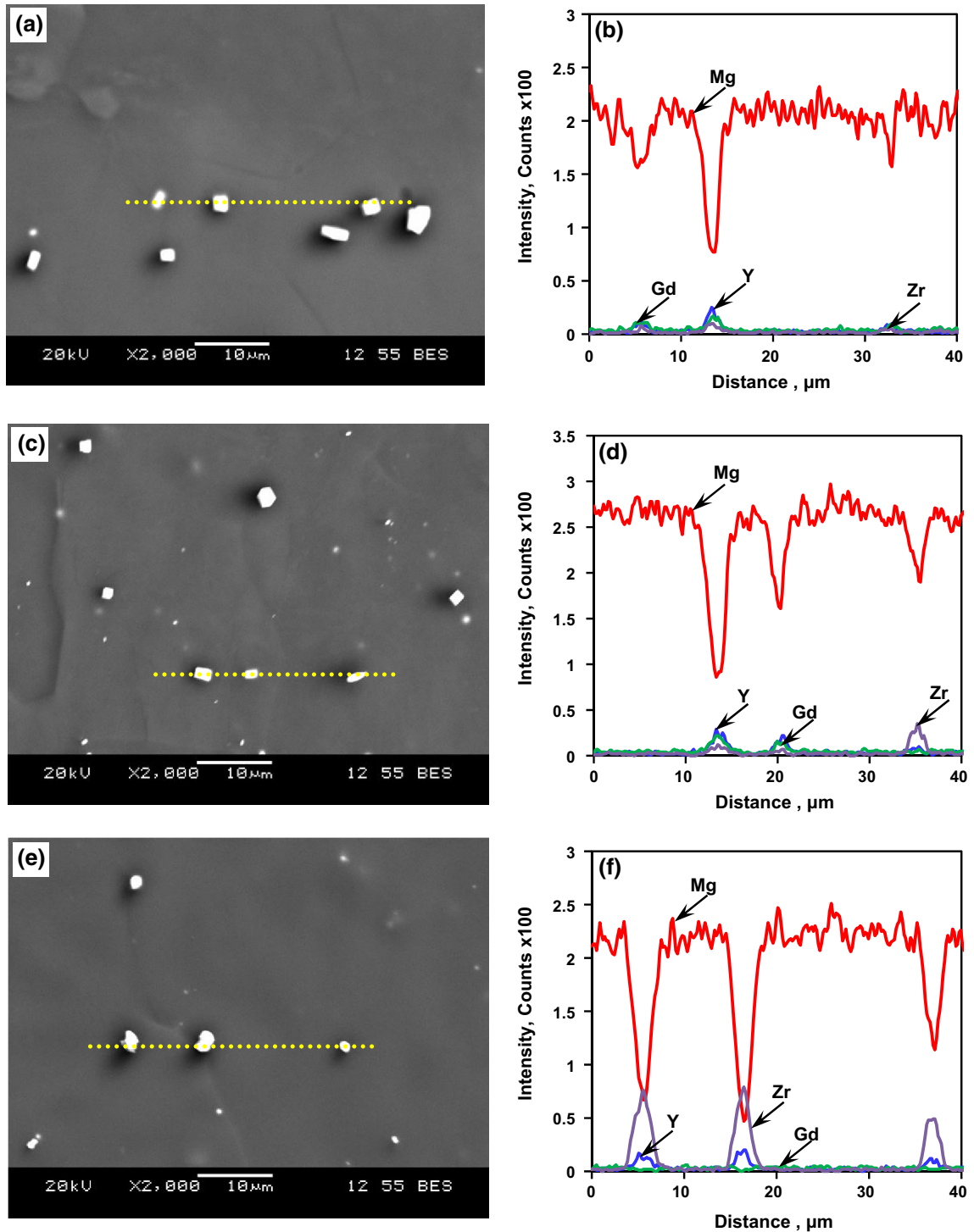


Fig. 2—SEM back-scattered electron images indicating EDS line scan positions and the corresponding EDS line scan results of GW103K alloy the (a) and (b) as-extruded, (c) and (d) T5, and (e) and (f) T6 conditions.

Mg-3.1 pct Y-11.7 pct Gd-0.3 pct Zr (in wt pct), respectively. A similar type of microstructures was also reported in the RE containing extruded Mg alloys in the literature, *e.g.*, Mg-11.90Gd-0.81Y-0.44Zr alloy by Zhang *et al.*,^[49] Mg-10Gd-3Y-0.5Zr by Liu *et al.*,^[50] and Mg-10Gd-3Y-0.5Zr and Mg-10Gd-3Y-1.0Zn-0.5Zr alloys by Liu *et al.*^[8] In addition, EDS line scan was performed as shown in Figures 2(a) and (b) which also

confirmed the presence of RE-rich particles in the as-extruded alloy, where all the regular (squared, rectangular, *etc.*) shaped particles contained all three major alloying elements of Gd, Y, and Zr.

The optical and SEM back-scattered electron images of T5 alloy are shown in Figures 1(c) and (d). The average grain size of the T5 alloy was about 25 μm which was almost doubled in comparison with the

as-extruded alloy, which indicates grain growth in the aging process at 498 K (225 °C) for 16 hours. Similar to the as-extruded alloy, RE-rich particles can also be seen from Figure 1(d). By means of EDS point analysis, the contents at points A and B of Figure 1(d) were estimated to be 69.2 pct Mg-17.3 pct Gd-13.2 pct Y, and 88.0 pct Mg-1.2 pct Y-9.7 pct Gd-1.2 pct Zr (in wt pct), respectively. It is clear from the point analysis that the particles in the T5 alloy had more or less the same composition as those in the as-extruded alloy. The EDS line scan was also conducted to confirm the presence of RE-rich particles as shown in Figures 2(c) and (d). However, as seen from Figure 2(d) the intensity of Zr-rich particles (irregular shaped particles as shown in Figure 2(c)) seemed to be higher as compared to the regular RE-rich particles in the as-extruded alloy due to the aging process. Wang *et al.*^[51] also reported that the square-shaped second particles were mostly rich with Gd and Y and round-shaped second particles were rich with Zr, which actually concurred the results of the GW103K alloy in both as-extruded and T5 states.

Figures 1(e) and (f) show the microstructures of T6 alloy. As shown in Figure 1(e), the average grain size became about 92 μm which was over three times larger than that in the T5 alloy, which indicates a marked grain growth due to the solution treatment at 773 K (500 °C) for 2 hours. Similar grain growth has been reported for Mg-10Gd-3Y alloy in the T4 and T6 conditions by Dong *et al.*^[35] and Liu *et al.*^[52] It can also be seen from Figure 1(f) that relatively fewer particles were present in the T6 state as compared with the as-extruded and T5 states. The contents at points A and B of Figure 1(f) were estimated to be 12.8 pct Mg-45.8 pct Gd-40.5 pct Y-1 pct Zr, and 67.7 pct Mg-12.3 pct Y-18.7 pct Gd-1.3 pct Zr (in wt pct), respectively. The EDS line scan results (Figures 2(e) and (f)) show that mainly round-shaped particles containing more Zr appeared in the T6 state. Similar observations were also reported by Wang *et al.*^[51] Based on the Mg-Gd phase diagram^[53] and Mg-Y phase diagram,^[54] only one single phase solid solution should appear in the Mg-10Gd-3Y-0.5Zr (GW103K) alloy during solution treatment at 773 K (500 °C). It was reported that the solubility of Gd and Y in Mg at 773 K (500 °C) was about 20 and 10 wt pct, respectively,^[53,54] whereas the solubility of Zr in Mg was very limited.^[55] This suggests that most of the Gd and Y particles could be dissolved into the matrix during the solution treatment at 773 K (500 °C) for 2 hours as seen from Figure 2(f), leaving a relatively high Zr-rich particles (round-shaped particles in Figure 2(e)) and more discernible Zr peaks (Figure 2(f)). In addition, RE-enrichment particles were also identified by three zone-axis electron microdiffraction patterns *via* TEM in the T6 alloy, as shown in Figure 3. Electron microdiffraction pattern in Figure 3(b) indicates the structure of particle A in Figure 3(a) which was identified as a cuboid-shaped (RE-rich) particle (face-centered cubic, fcc with $a = 0.56$ nm). Similar results were reported in the cast-T6 samples of Mg-10Gd-2Y-0.5Zr alloy by He *et al.*,^[31] Mg-Gd-Nd-based alloy during solution treatment by Khawaled *et al.*,^[56] cast T6 samples of Mg-4Y-2Nd-1Gd-0.4Zr alloy by Liu *et al.*,^[57] and Mg-9Gd-2Er-

0.4Zr alloy after solution treatment by Wang *et al.*^[58] Figures 3(c) and (d) show the TEM micrographs recorded from the sample after peak-aging at 498 K (225 °C) for 16 hours, with the incident electron beam approximately parallel to $[0001]_z$. A large number of high density of bamboo-leaf/plate-shaped precipitates with a diameter less than 15 nm formed and distributed uniformly in the matrix, as shown in Figure 3(c). Such precipitates were identified by selected area electron diffraction (SAED) analysis to be a β' phase which had a c -based centered orthorhombic structure (cbco) ($a = 2 \times a_{z\text{-Mg}} = 0.64$ nm, $b = 8 \times d(10\bar{1}0)_{z\text{-Mg}} = 2.22$ nm, $c = c_{z\text{-Mg}} = 0.52$ nm).^[31,59,60] The composition of β' phase was determined to be approximately $\text{Mg}_7(\text{Gd},\text{Y})$ as reported by Gao *et al.*^[61] and Nishijima *et al.*^[62] A similar type of precipitates has also been reported in the cast T6 samples of Mg-10Gd-2Y-0.5Zr alloy by He *et al.*,^[31] solution-treated and aged Mg-10Gd-3Y-0.4Zr alloy by He *et al.*,^[59] and solution-treated and aged Mg-15Gd-0.5Zr alloy by Gao *et al.*^[60]

Figure 4 shows the crystallographic textures (basal (0001), prismatic (10 $\bar{1}0$), and pyramidal (10 $\bar{1}1$) pole figures) of the GW103K alloy in different states (as-extruded, T5, and T6 conditions) evaluated using MTEX software, where ED stands for the ED and RD denotes the radial direction. As seen from Figure 4, relatively weaker textures (with a maximum intensity of 2.1 multiples of random distribution (MRD)) for the as-extruded, 3.3 MRD for the T5, and 4.5 MRD for the T6 samples were observed after the defocusing correction, in comparison with the extruded AM30^[14] and rolled AZ31.^[63] This was basically in agreement with the study by Liu *et al.*,^[52] where the intensity of the T5 and T6 textures was stronger than that of the extruded alloy. The presence of such weaker textures in the RE-Mg alloy was a major benefit of adding RE elements into Mg alloys, as also reported by Stanford and Barnett^[64] who observed that microalloying with RE elements could weaken texture in the forming process. It was also reported that an addition of small amount of Gd^[65] and Ce^[28] to Mg alloys could significantly reduce the texture of the extruded alloy and the addition of Y element had a similar effect on the texture of Mg alloys.^[66] Furthermore, Bohlen *et al.*^[34] reported that the overall texture intensity and the basal pole intensity aligned with the sheet normal direction were lower in the RE-containing alloys than in the conventional alloys. Similar weaker texture in the Mg-based alloys with the addition of RE elements was also reported in References 15, 18 through 20, 33, 34.

In the as-extruded sample (Figure 4(a)^[17]), it can be seen that the c -axes of hcp unit cells in most grains were oriented towards the radial direction (RD), as indicated by the basal (0001) pole distribution, along with the prismatic (10 $\bar{1}0$) and pyramidal (10 $\bar{1}1$) poles towards the ED. In the T5 sample (Figure 4(b)), while the c -axes of most grains were oriented towards the RD, a slight change of the basal (0001) pole has been observed, *i.e.*, the basal (0001) pole intensity at the center was became higher. It is also seen from the Figure 4(b) that similar to the as-extruded sample (Figure 4(a)^[17]), the prismatic (10 $\bar{1}0$) and pyramidal (10 $\bar{1}1$) poles towards the ED, which indicates that the textures of T5 samples basically

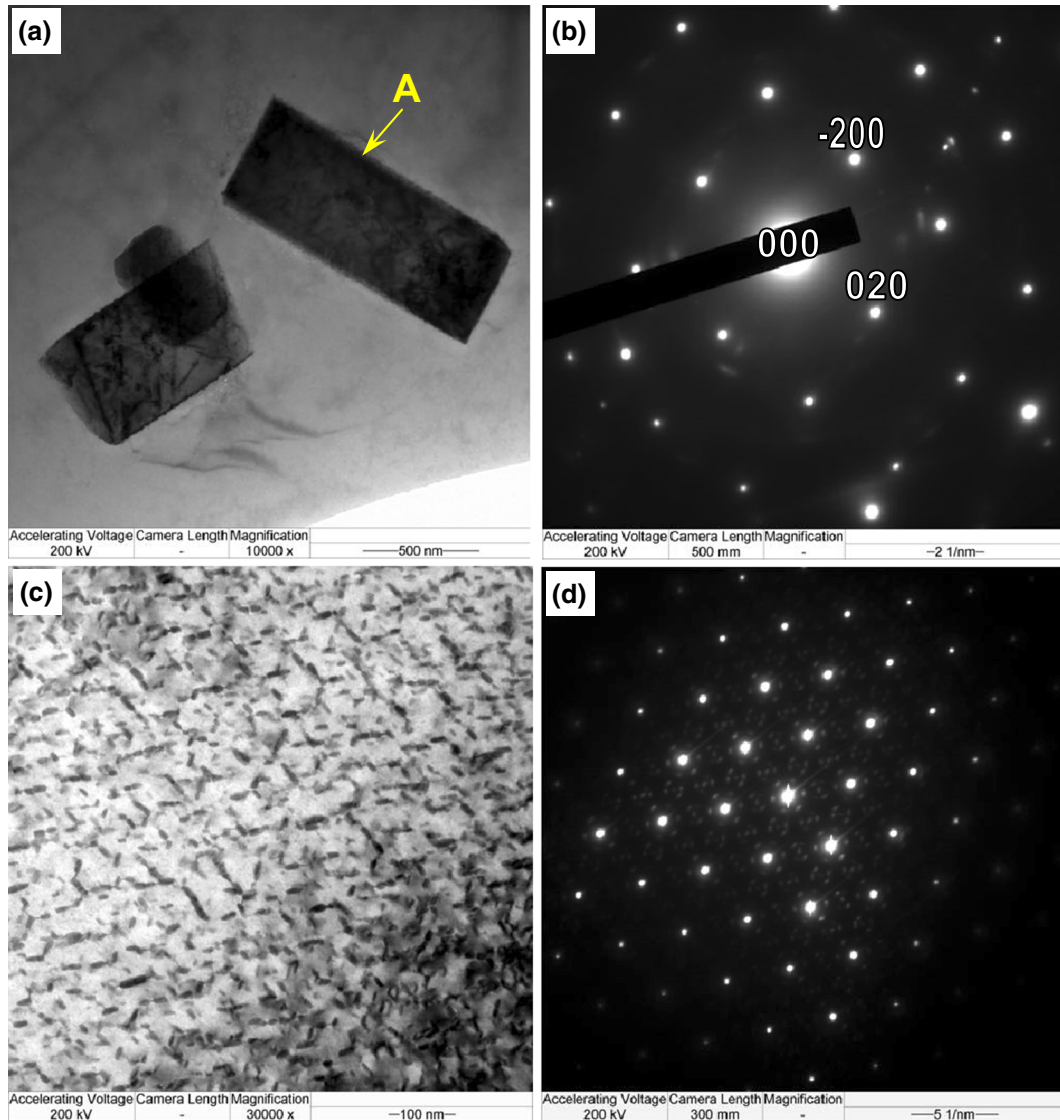


Fig. 3—Transmission electron micrographs recorded from a sample of T6 alloy: (a) bright-field image taken along [001] zone axis of particle A, (b) [001] zone axis microdiffraction pattern recorded from particle A, (c) bright-field images taken along [0001]_z zone axis, and (d) the corresponding SAED patterns shown in B//[0001]_z.

tried to retain during the aging process and the components seemed elongated in the RD. This elongation was more expected in the RE containing alloy rather than in the standard alloy AZ31.^[20] Similar tendency of retaining textures has been reported for Mg-10Gd-3Y Mg alloy after T5 aging treatment at 498 K (225 °C) for 4, 10, and 150 hours by Liu *et al.*,^[52] for cast Mg-1Zn-0.3Ce (ZE10) alloy after annealing treatment at 673 K (400 °C) for 15 minutes by Machenzie and Pekguleryuz,^[67] and for as-extruded AZ31 alloy after annealing treatment at 723 K and 793 K (450 °C and 520 °C) for 30 minutes, 3, and 17 hours by Perez-Prado and Ruano.^[68] The textures in the T6 sample (Figure 4(c)) exhibited a greater spread of basal (0001) pole around the RD as compared with other two alloys (as-extruded and T5). However, the intensity variation of this T5 alloy was in contrast to that of Liu *et al.*,^[52]

where the variation of intensity was in a reversed order. Hirsch and Al-Samman^[33] also reported that the texture weakening occurred during recrystallization annealing. This difference was mainly due to the combined effects of RE elements and the precipitates formed during the heat treatment.

B. Tensile Properties

Typical tensile stress–strain curves of the GW103K alloy in different states tested at a strain rate of $1 \times 10^{-4} \text{ s}^{-1}$ is shown in Figure 5 and the tensile properties obtained are listed in Table I. As seen from Table I, the present GW103K alloy (as-extruded, T5, and T6) exhibited a higher tensile yield strength (YS) than the RE-free extruded AM30 alloy, *i.e.*, ~232, 332, and 342 *vs* ~189 MPa as reported in Reference 11. This

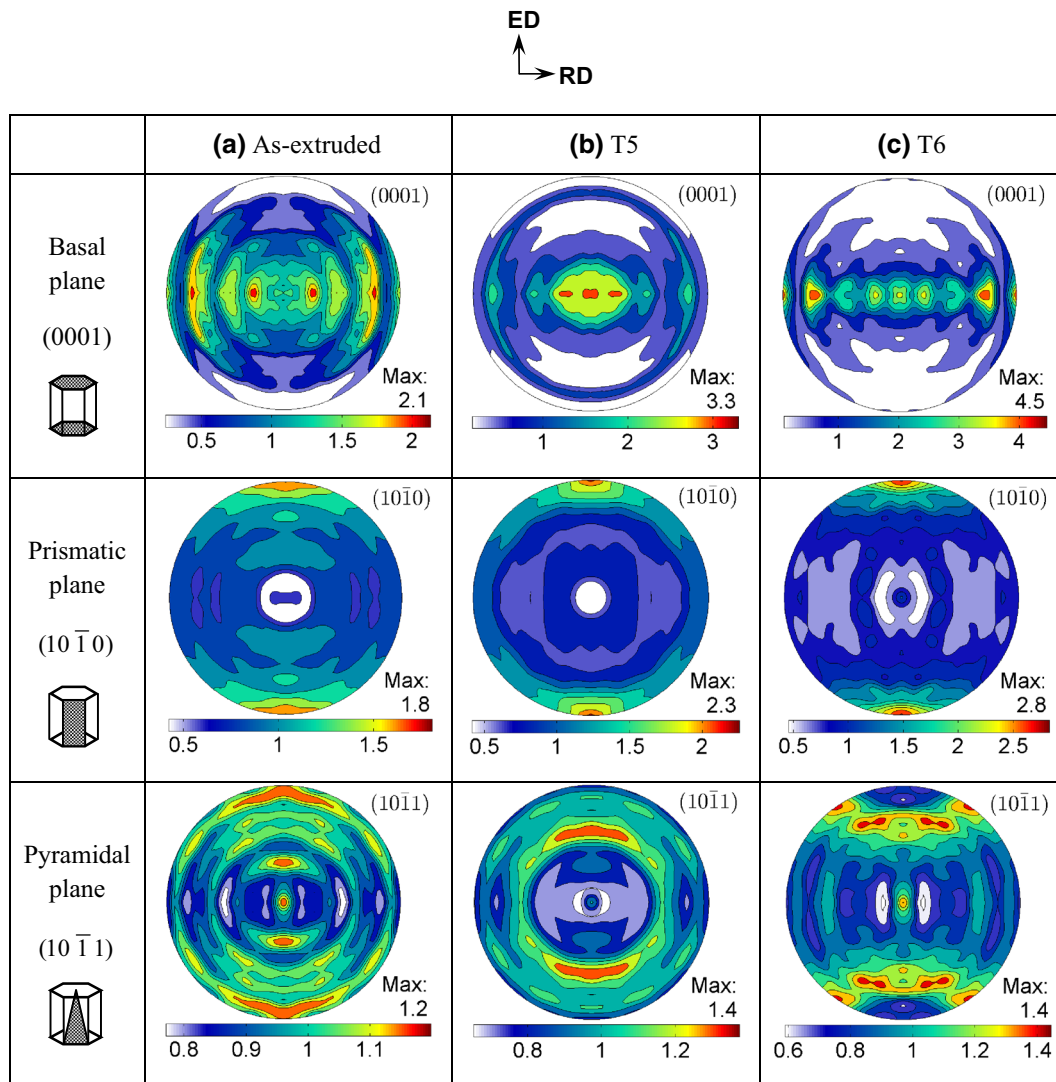


Fig. 4—Pole figures of basal (0001) plane, prismatic ($10\bar{1}0$) plane, and pyramidal ($10\bar{1}1$) plane of GW103K alloy in the (a) as-extruded,^[17] (b) T5, and (c) T6 states, where ED indicates the extrusion direction and RD denotes the radial direction.

indicated an obvious beneficial role of RE element addition in the Mg alloy, which was in agreement with those in an extruded Mg-8Al-xRE alloy,^[69] where the improved tensile properties due to the addition of RE elements were reported as well. As seen from Figure 5 and Table I, in comparison with the as-extruded alloy, significant improvements in the yield strength (YS) and ultimate tensile strength (UTS) were attained in the T5 alloy, by approximately 100 and 108 MPa, respectively. Similar results were reported in the T5 samples of Mg-10Gd-2Y-0.5Zr alloy by He *et al.*,^[31] T5 samples of Mg-10Gd-3Y alloy by Liu *et al.*,^[52] T5 samples of Mg-10Gd-3Y-0.5Zr alloy by Liu *et al.*,^[8] and extruded samples of Mg-10Gd-3Y-0.5Zr alloy by Yang *et al.*,^[15] where a significant improvement in the YS and UTS was seen after the T5 aging treatment as well. However, the percent elongation of the T5 alloy (6.6 pct) decreased by about 20 pct as compared with that of the as-extruded alloy (8.3 pct). These results were due to the precipita-

tion hardening as seen in Figure 3 and also reported in References 31, 57. As seen from Table I, a further improvement in the YS (about 110 MPa) and UTS (about 112 MPa) was achieved *via* the T6 heat treatment as compared with the as-extruded alloy. Similar improvements in the YS and UTS in the T6 alloy have been reported by Liu *et al.*^[57] The percent elongation of the T6 alloy decreased more as compared with that of the as-extruded alloy. The relatively small difference between the T5 and T6 states, as seen from Figure 5 and Table I, was a consequence of a combined role of grain size and precipitates. While the T6 heat treatment would lead to a more complete precipitation hardening due to the formation of the supersaturated solid solution in the solution treatment phase prior to aging, the much larger grain size (Figures 1(e) and (f)) due to the same solution treatment caused a certain extent of sacrifice or cutback in the strength based on the well-known Hall-Petch relationship^[70] and in the ductility as well.

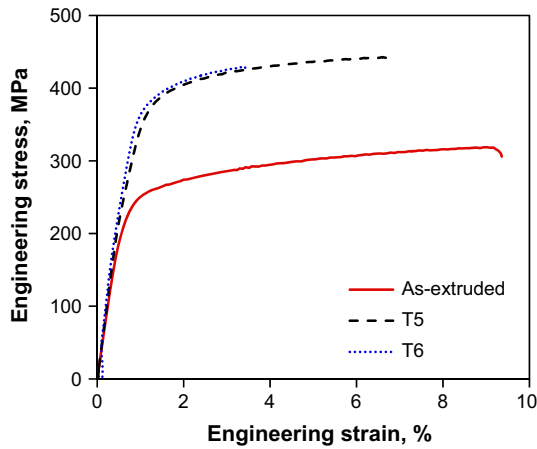


Fig. 5—Typical tensile stress–strain curves of the GW103K alloy in different conditions tested at a strain rate of $1 \times 10^{-4} \text{ s}^{-1}$.

Table I. Tensile Properties of GW103K Alloy in Different States Obtained at a Strain Rate of $1 \times 10^{-4} \text{ s}^{-1}$

Materials	σ_{YS} (MPa)	σ_{UTS} (MPa)	Elongation (pct)	n
As-extruded	232	318	8.3	0.15
T5	332	426	6.6	0.19
T6	342	430	3.2	0.17

C. Hysteresis Loops

Figure 6 shows typical stress–strain hysteresis loops of the first, second, and mid-life cycles at a total strain amplitude of 1.2 pct and strain ratio of $R_\epsilon = -1$ for the GW103K alloy in different states. It is seen from Figure 6(a) that, like the tensile stress–strain curves (Figure 5), the initial slope in the ascending phase of the first cycle was the same in all the three alloy states, indicating that the T5 and T6 heat treatment did not affect the Young’s modulus of the alloy. As normally anticipated, heat treatment would alter the strength of a material, but had little influence on the Young’s modulus, since the magnitude of Young’s modulus is a measure of the resistance to separation of adjacent atoms, *i.e.*, interatomic bonding forces on an atomic scale. The present GW103K alloy was observed to exhibit nearly symmetrical hysteresis loops in all the three alloy conditions, which were somewhat similar to those of face-centered cubic (fcc) metals (*e.g.*, Al, Cu, Ni) as a result of the dislocation slip-dominated deformation in most materials.^[71] This was, however, in contrast to the hysteresis loops in the rare earth-free extruded or rolled Mg alloys, where the hysteresis loops were very asymmetrical due to the presence of strong crystallographic texture.^[10–13] The maximum and minimum peak stresses in the T5 and T6 conditions showed a significant enhancement in different loops as compared with those in the as-extruded GW103K alloy, due to the presence of a large number of precipitates after the T5 and T6 heat treatment (Figure 3). Similar to the tensile properties shown in Figure 5 and Table I, the T6 alloy exhibited only a slightly higher maximum and minimum

peak stresses than the T5 alloy (Figure 6). Unlike the fcc metals where the slope of hysteresis loops after the strain reversal either at the maximum or minimum stress was basically equal to the value of Young’s modulus, the pseudoelastic or nonlinear elastic behavior in both descending and ascending phases in the RE containing GW103K alloy was still in existence, in spite of the symmetrical hysteresis loops. It seemed reasonable to consider that the pseudoelastic behavior would be an inherent characteristic of Mg alloys, as it originated from reversible movement of dislocations, twinning, and stress-induced phase transformation,^[72] which was related to the superior damping capacity. Further studies in this aspect are needed. However, in comparison with the as-extruded Mg alloy,^[10–13,17] the pseudoelastic behavior reduced to a certain extent in the GW103K alloy, especially in the T5 and T6 conditions.

D. Cyclic Deformation Response

Figure 7 shows the evolution of cyclic stress amplitude as a function of the number of cycles at different strain amplitudes on a semi-log scale for the GW103K alloy in the (a) as-extruded,^[17] (b) T5, and (c) T6 states, respectively. It is seen that as the applied total strain amplitude increased, the cyclic stress amplitude increased and the fatigue life decreased for the GW103K alloy in all states. Unlike the RE-free extruded alloys, *e.g.*, AM30^[11] and AZ31^[10,12,13] where cyclic stabilization occurred only at lower strain amplitudes of about 0.1 and 0.2 pct, the as-extruded GW103K alloy exhibited cyclic stabilization until failure up to a strain amplitude of 1.0 pct. Even at a strain amplitude of 1.2 pct for the as-extruded alloy, only slight change, *i.e.*, an initial slight cyclic hardening within the first three cycles and then minor cyclic softening, could be seen from Figure 7(a), which corresponded well to the variation of the plastic strain amplitude ($\Delta\epsilon_p/2$) during cyclic deformation as shown in Figure 8(a) for different total strain amplitudes.^[17] This was due to the addition of RE elements which significantly changed the microstructure (Figures 1 and 3) and weakened the texture (Figure 4). For the heat-treated T5 and T6 states, cyclic stabilization occurred up to a strain amplitude of 0.6 pct (Figures 7(b) and (c)), which was followed by the slight cyclic hardening at the higher strain amplitudes (0.8 to 1.2 pct). These also corresponded well to the decreasing plastic strain amplitude (Figures 8(b) and (c)). However, while the initial cyclic deformation characteristics were similar for the alloy in different states, the cyclic stress amplitudes and also plastic strain amplitudes at a given total strain amplitude applied were different, except at the lower strain amplitudes (0.2 and 0.4 pct). For example, at a given total strain amplitude of 0.8 pct, the stress amplitudes were ~ 240 , ~ 290 , and ~ 300 MPa for the as-extruded, T5, and T6 samples, respectively (Figure 7). The difference in the stress amplitudes also increased at higher strain amplitudes. For the plastic strain amplitudes, at a given total strain amplitude of 0.8 pct, the values were ~ 0.2 , ~ 0.165 , and ~ 0.11 pct for the as-extruded, T5, and T6 samples, respectively (Figures 8(a) through (c)^[17]).

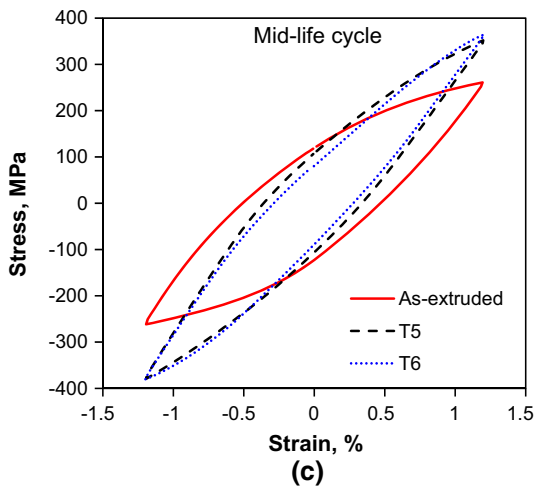
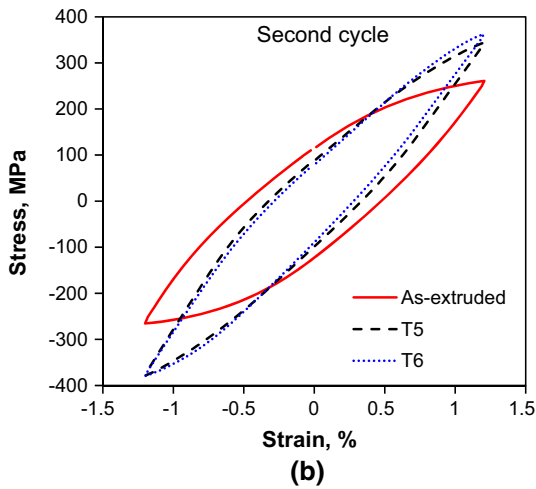
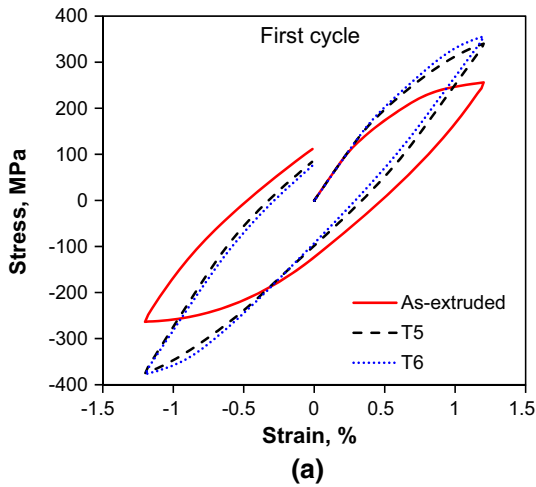


Fig. 6—Typical stress-strain hysteresis loops of GW103K alloy in different states tested at a given total strain amplitude of 1.2 pct and strain ratio of $R_\epsilon = -1$ of (a) first cycle, (b) second cycle, and (c) mid-life cycle.

E. Fatigue Life and Fatigue Parameters

The fatigue life (*i.e.*, the number of cycles to failure, N_f) as a function of the applied total strain amplitudes ($\Delta\epsilon_t/2$) of the GW103K alloy in the as-extruded, T5,

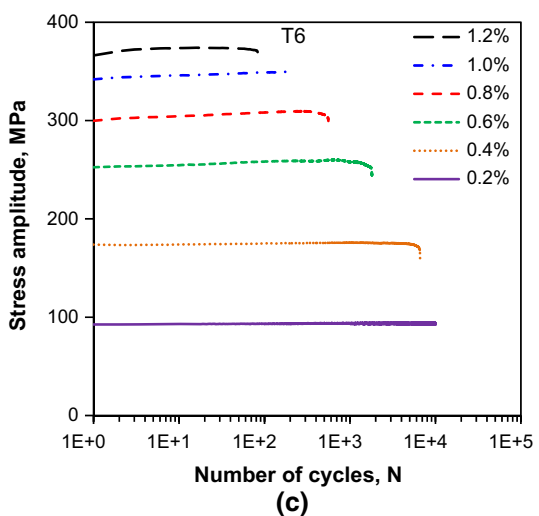
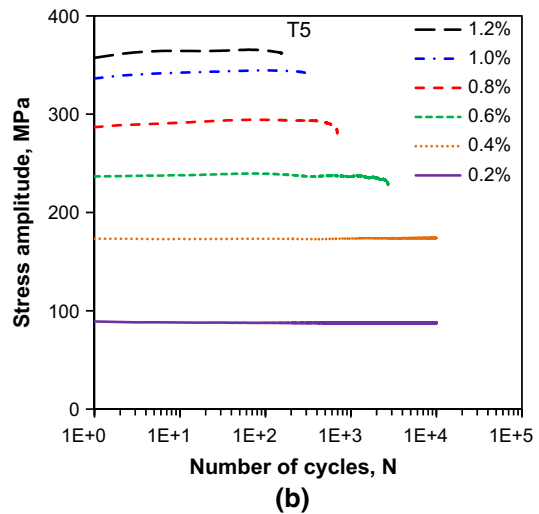
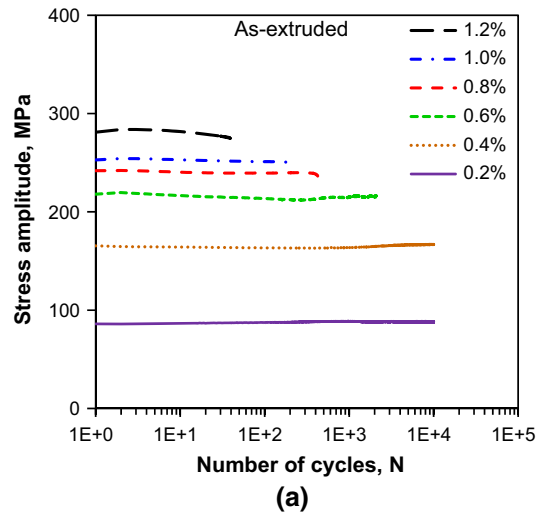


Fig. 7—Stress amplitude vs the number of cycles at different total strain amplitudes applied for the GW103K alloy in the (a) as-extruded,^[17] (b) T5, and (c) T6 states.

and T6 states is shown in Figure 9, along with the experimental data reported in the literature for various extruded Mg alloys^[11,12,17,63,73–75] for comparison. The

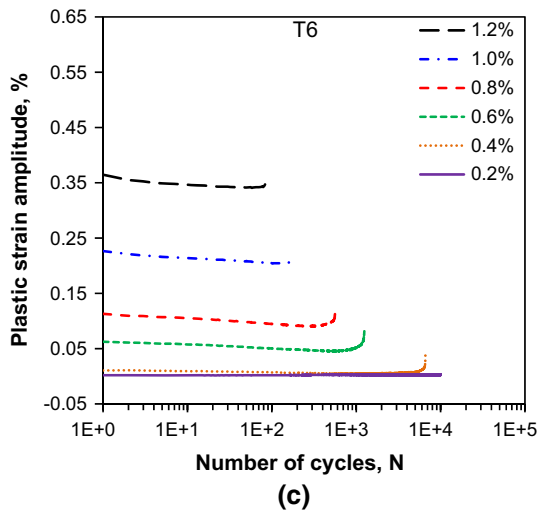
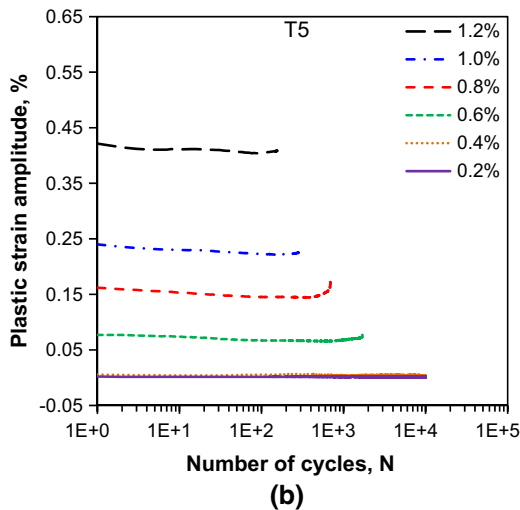
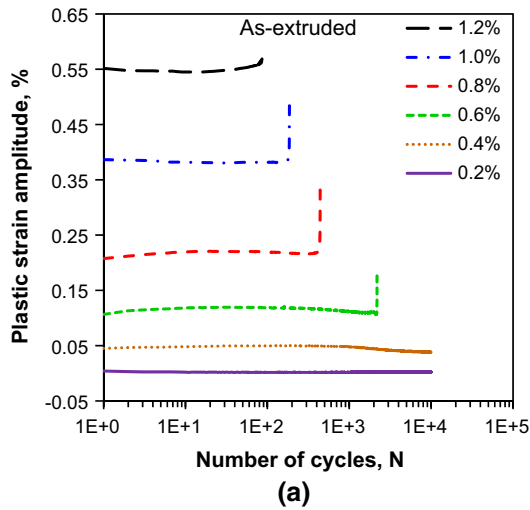


Fig. 8—Plastic strain amplitude vs the number of cycles at different total strain amplitudes applied for the GW103K alloy in the (a) as-extruded,^[17] (b) T5, and (c) T6 states.

run-out data points were indicated by arrows pointing horizontally at or over 10^7 cycles. The present GW103K alloy showed a trend of increasing fatigue life with

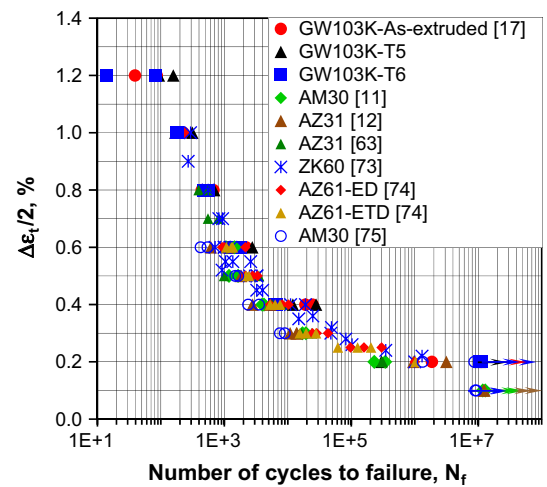


Fig. 9—Total strain amplitude vs the number of cycles to failure for the GW103K alloy in the as-extruded, T5, and T6 states, in comparison with the data reported in the literature for various extruded Mg alloys.^[11,12,17,63,73–75]

decreasing strain amplitude in all conditions and there was no significant difference in the fatigue lives among the different alloy states. Overall, the alloy basically showed an improved fatigue life than the RE-free extruded Mg alloys.^[11,12,63,73–75] Based on the Basquin's equation and Coffin-Manson relation and as described in References 10, 12, 13, 70, 76, 77, the total strain amplitude could be expressed as two parts of elastic strain amplitude and plastic strain amplitude, *i.e.*,

$$\frac{\Delta \epsilon_t}{2} = \frac{\Delta \epsilon_e}{2} + \frac{\Delta \epsilon_p}{2} = \frac{\sigma'_f (2N_f)^b}{E} + \epsilon'_f (2N_f)^c, \quad [1]$$

where E is the Young's modulus (for the present alloy, the average value obtained during fatigue testing was ~ 44.5 GPa), N_f is the fatigue life or the number of cycles to failure, σ'_f is the fatigue strength coefficient, b is the fatigue strength exponent, ϵ'_f is the fatigue ductility coefficient, and c is the fatigue ductility exponent. In addition, cyclic deformation behavior is normally considered to be related to the portion of the plastic strain amplitude and is independent of the elastic strain amplitude, which could be expressed by the following equation,^[10]

$$\frac{\Delta \sigma}{2} = K' \left(\frac{\Delta \epsilon_p}{2} \right)^{n'}, \quad [2]$$

where $\frac{\Delta \sigma}{2}$ is the mid-life stress amplitude, $\frac{\Delta \epsilon_p}{2}$ is the mid-life plastic strain amplitude, n' is the cyclic strain-hardening exponent, and K' is the cyclic strength coefficient. The Coffin-Manson plot, together with the Basquin's relationship and the total strain amplitude as a function of the number of reversals to failure ($2N_f$) in the as-extruded, T5, and T6 states, are shown in Figure 10. As seen from Figure 10, when the strain amplitude (elastic, or plastic, or total value) was lower, the fatigue lifetime was longer; the experimental data obtained over a wide range of strain amplitudes followed both the Coffin-Manson and Basquin's relation-

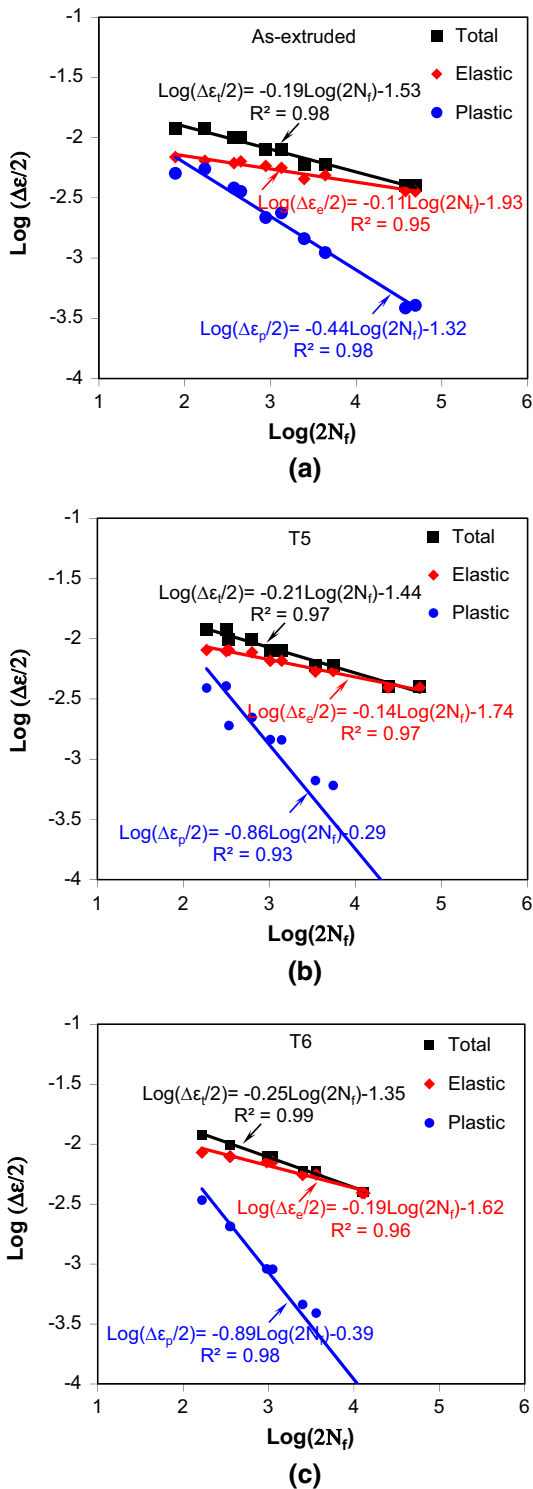


Fig. 10—Cyclic total, plastic, and elastic strain amplitude-fatigue life response of the GW103K alloy in the (a) as-extruded,^[17] (b) T5, and (c) T6 states.

ships well. In addition, the fatigue life parameters evaluated on the basis of Eqs. [1] and [2] are summarized in Table II. It is seen that while the obtained fatigue parameters were well within the range in other fatigued Mg alloys reported in the literature,^[10–12,78] the cyclic strain-hardening exponent n' of the GW103K

alloy was lower than that of RE-free Mg alloys.^[10–12,78] This corresponded well to the higher yield strength (Table I) and cyclic stabilization characteristics of these alloys (Figures 7 and 8). While the cyclic strain-hardening exponent (n') of T5 alloy was slightly lower than that of the as-extruded alloy, the cyclic strength coefficient (K') and fatigue strength coefficient (σ'_f) of the T5 alloy were higher than those of the as-extruded alloy, which corresponded well to their monotonic yield strength (*i.e.*, 332 MPa for the T5 sample *vs* 232 MPa for the as-extruded sample). Further improvements in the cyclic strength coefficient (K') and fatigue strength coefficient (σ'_f) were seen in the T6 alloy as compared to those of the as-extruded alloy (Table II). The values of fatigue strength exponent (b) and fatigue ductility exponent (c) decreased in both T5 and T6 samples as compared to the as-extruded sample. In general, a smaller absolute value of fatigue strength exponent (b) and fatigue ductility exponent (c) and a larger value of fatigue strength coefficient (σ'_f) and fatigue ductility coefficient (ϵ'_f) reflect a longer fatigue life.^[79–82] This indeed implies that a longer fatigue life of a material in the strain-controlled fatigue tests requires a good combination of both higher strength and superior ductility. In spite of such a seemingly conflicting effect of the exponent pair (b and c) and the coefficient pair (σ'_f and ϵ'_f) on the fatigue life, the exponent pair would be expected to play a more significant role in the sense of exponential functions (Eq. [1]).^[79] In comparison with the as-extruded alloy, the absolute values of b and c in both T5 and T6 states were higher, but the values of σ'_f and ϵ'_f were higher as well. As a result, a coupled role of these fatigue-life prediction parameters listed in Table II would give an equivalent lifetime of the GW103K alloy in different states within the experimental scatter, as shown in Figure 9,^[17] which was in general longer than that of RE-free extruded Mg alloys. It should be noted that in evaluating the above fatigue life parameters, the run-out data for the fatigue samples without failure at or above 10^7 cycles were not included. Furthermore, the obtained cyclic stress-strain curves corresponding to the mid-lives of the GW103K alloy in different conditions are shown in Figure 11 along with the monotonic stress-strain curves. It is seen that cyclic stress-strain curves were generally consistent with the monotonic ones for the GW103K alloy in different conditions within the experimental scatter. The obtained cyclic yield strength (σ'_{cy}) and cyclic strain-hardening exponent (n') of the GW103K alloy in different states were also equivalent to their respective monotonic yield strength and strain-hardening exponent, as seen from Tables I and II.

F. Fractography

Figure 12 shows an overall view of fracture surfaces of the GW103K alloy in different conditions at a total strain amplitude of 0.4 pct, containing fatigue crack initiation, propagation, and final fast fracture regions. It is seen from the low magnification images (Figure 12) that fatigue crack initiated basically from the specimen surface. Compared with the as-extruded and T5 samples, the fracture surfaces of the T6 sample were

Table II. Low-Cycle Fatigue Parameters Obtained for the GW103K Alloy in the As-Extruded, T5, and T6 Conditions

Low-Cycle Fatigue Parameters	As-Extruded	T5	T6
Cyclic yield strength, σ'_y (MPa)	215	305	350
Cyclic strain-hardening exponent (n')	0.19	0.16	0.20
Cyclic strength coefficient, K' (MPa)	734	897	1230
Fatigue strength coefficient, σ'_f (MPa)	518	811	1054
Fatigue strength exponent (b)	-0.11	-0.14	-0.19
Fatigue ductility coefficient, (ϵ'_f)	0.05	0.52	0.41
Fatigue ductility exponent (c)	-0.44	-0.87	-0.89

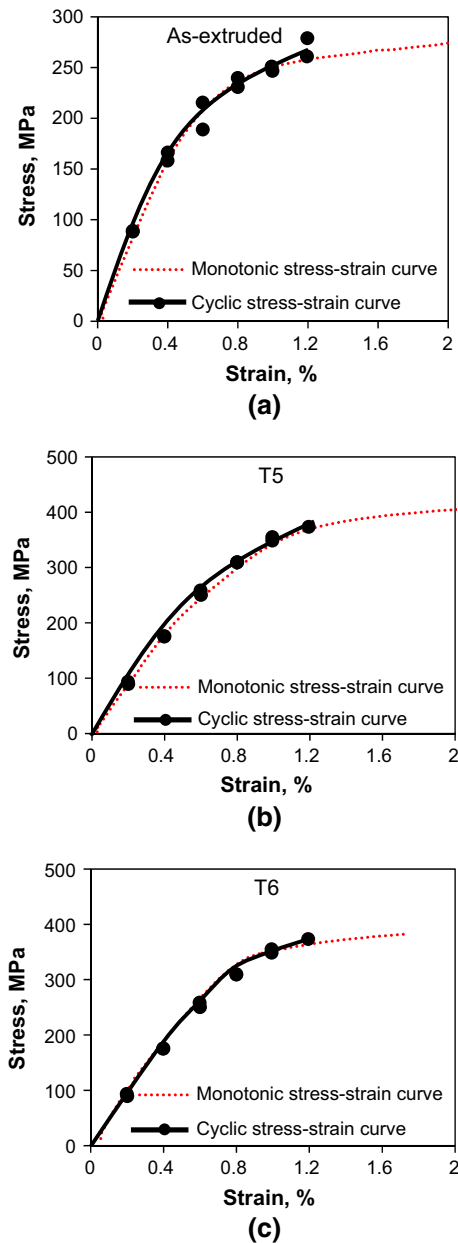


Fig. 11—Cyclic stress–strain curves for the GW103K alloy in the (a) as-extruded, (b) T5, and (c) T6 states, where the corresponding monotonic stress–strain curves are also plotted for comparison.

obviously rougher because of the larger grain size (Figures 1(e) and (f)). Figure 13 shows the fractographs near the crack initiation site and in the crack propaga-

tion area of the fatigued samples at higher magnifications. In the near-initiation area (as indicated by the red-dashed box in Figure 12), typical flow lines or tearing ridges indicating fatigue crack growth direction could be seen in both as-extruded and T5 samples as shown in Figures 13(a) and (c), respectively. Fatigue crack propagation region was basically characterized by the fatigue striations which were perpendicular to the crack propagation direction as shown in Figures 13(b) and (d) for the as-extruded and T5 samples, respectively. However, a mix of cleavage-like features and tearing ridges in the near-initiation area on the fracture surface of the T6 sample fatigued at a strain amplitude of 0.4 pct can be seen from Figure 13(e). A three-dimensional image taken in the propagation area is shown in Figure 13(f), with a main feature of fatigue striations as well. Similar fracture surface features consisting of a mix of cleavage-like features, tearing ridges, and fatigue striations were reported in the T6 GW103 alloy by Dong *et al.*^[35] It was also observed that the spacing of fatigue striations became progressively larger with increasing distance from the crack initiation site. Since each fatigue striation could be assumed to roughly represent a single loading cycle, the spacing of fatigue striations could reflect the fatigue crack propagation rate and the associated fatigue life.^[79] It is known that the occurrence of fatigue striations was due to a repeated plastic blunting-sharpening process in face-centered cubic (fcc) materials arising from the slip of dislocations in the plastic zone in front of the fatigue crack tip.^[83] The formation of the fatigue striations in the HCP Mg alloy was anticipated to be related to both dislocation slip and twinning in the plastic zone during fatigue crack propagation.^[10–13] Unlike the as-extruded and T5 samples, crack propagation near initiation in the T6 sample shown in Figures 12(c) and 13(e) appeared fairly different. To make sure where the crack initiation was, two different regions as indicated by the yellow-dashed boxes in Figure 12(c) were examined in more detail and shown in Figure 14. The region close to the upper left corner had fatigue striations coupled with the cleavage-like facets (Figures 14(a) and (b)), while no sign of fatigue striations could be identified in the region near the lower right corner (Figures 14(c) and (d)). Thus, fatigue crack initiation in the T6 sample was confirmed to be from the upper left corner (as indicated by the red-dashed box in Figure 12(c)) rather than from the seemingly flatter surface at the lower right corner. The occurrence of the cleavage-like features was likely to be associated with the much larger grain size (Figures 1(e) and (f)) stem-

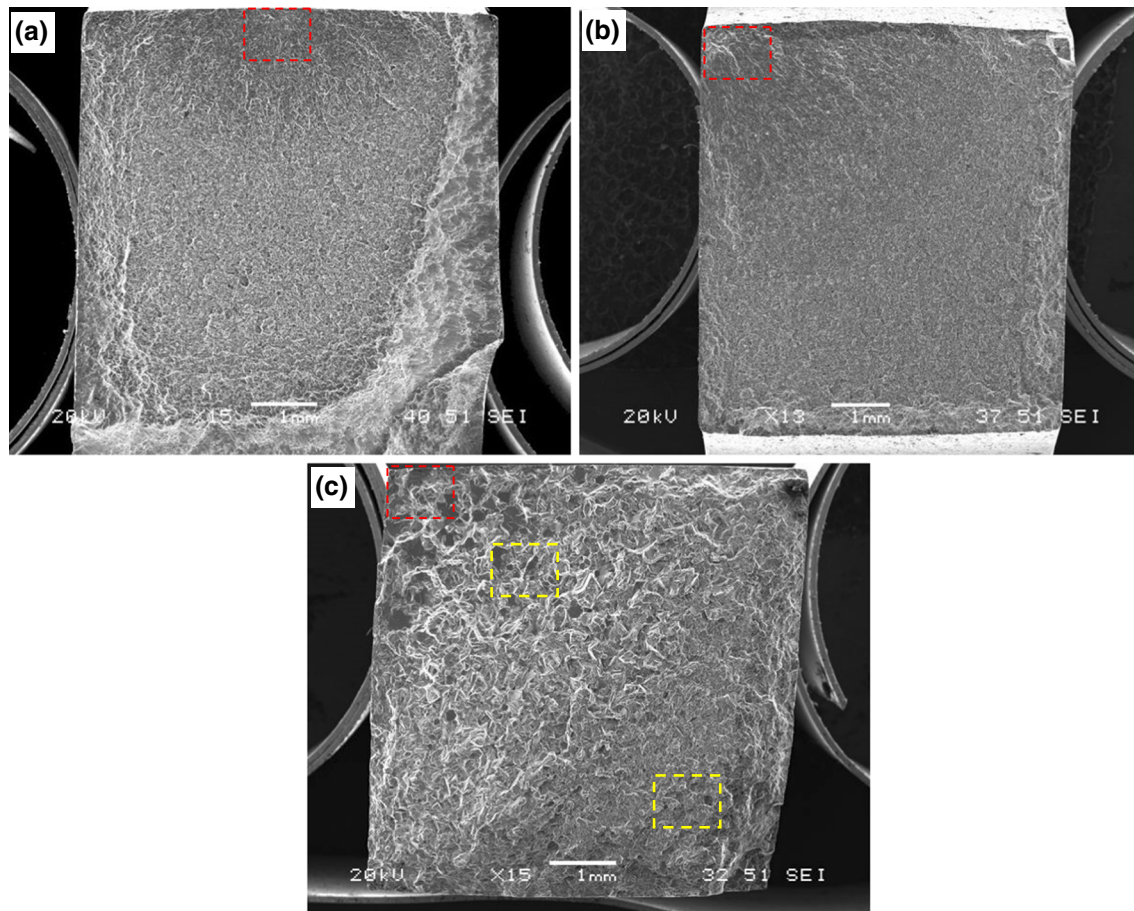


Fig. 12—An overall view of fracture surfaces fatigued at a strain amplitude of 0.4 pct of the GW103K alloy in the (a) as-extruded,^[17] (b) T5, and (c) T6 states (Color figure online).

ming from the relatively high solution temperature at 773 K (500 °C) for 2 hours.

IV. DISCUSSION

A. Effect of Heat Treatment on Tensile Properties

The mechanical properties of alloys are known to be dependent on the alloying elements and the resulting microstructures including fine precipitates that appear after proper heat treatment. The process of adding other elements to a metal to increase its strength is commonly referred to as solid solution (or solute) strengthening. The effect of these solutes (or impurity atoms) is to obstruct the movement of dislocations. Edge dislocations for example can result in internal pressures in a crystal through the distortion of the periodic lattice. In the presence of impurity atoms with a larger atomic radius, dilatational stresses are lowered and the energy of the system is decreased if the solute atoms are positioned below the edge dislocations. Therefore, extra stress is required to move dislocations away from the solute atom, which impedes their movement.^[84] As seen from the periodic table, all RE elements including both series of lanthanides and actinides have an atomic radius

larger than that of Mg. Also, the solid solution of the RE elements in Mg is relatively high, *e.g.*, Gd could dissolve up to 3.8 wt pct at about 473 K (200 °C) to replace the Mg atoms and form a substitutional solid solution.^[85] Since the RE element (Gd and Y) atoms as well as Zr atoms in the present GW103K alloy are all larger than Mg atoms, squeezing them into the Mg lattice would not only generate compressive stresses imposed on the nearby host atoms but also roughen the slip plane, thus make it more difficult for dislocations to move. It follows that the addition of RE elements to Mg even in the form of solid solution alone would improve the resistance to the motion of dislocations, and thereby increasing the yield strength. This would be the main reason why a fairly high strength of GW103K in the as-extruded state is observed (Table I).

Regarding the precipitation strengthening, an alloy containing an adequate volume fraction of fine particles of an impurity phase through heat treatment will have a higher strength, due to the impediment of particles to the movement of dislocations. In the RE-Mg alloys fine and evenly oriented (the planes parallel to the prismatic or basal planes of Mg matrix) and uniformly distributed particles can improve the tensile properties.^[86] On the other hand, Yin *et al.*^[87] reported that relatively large

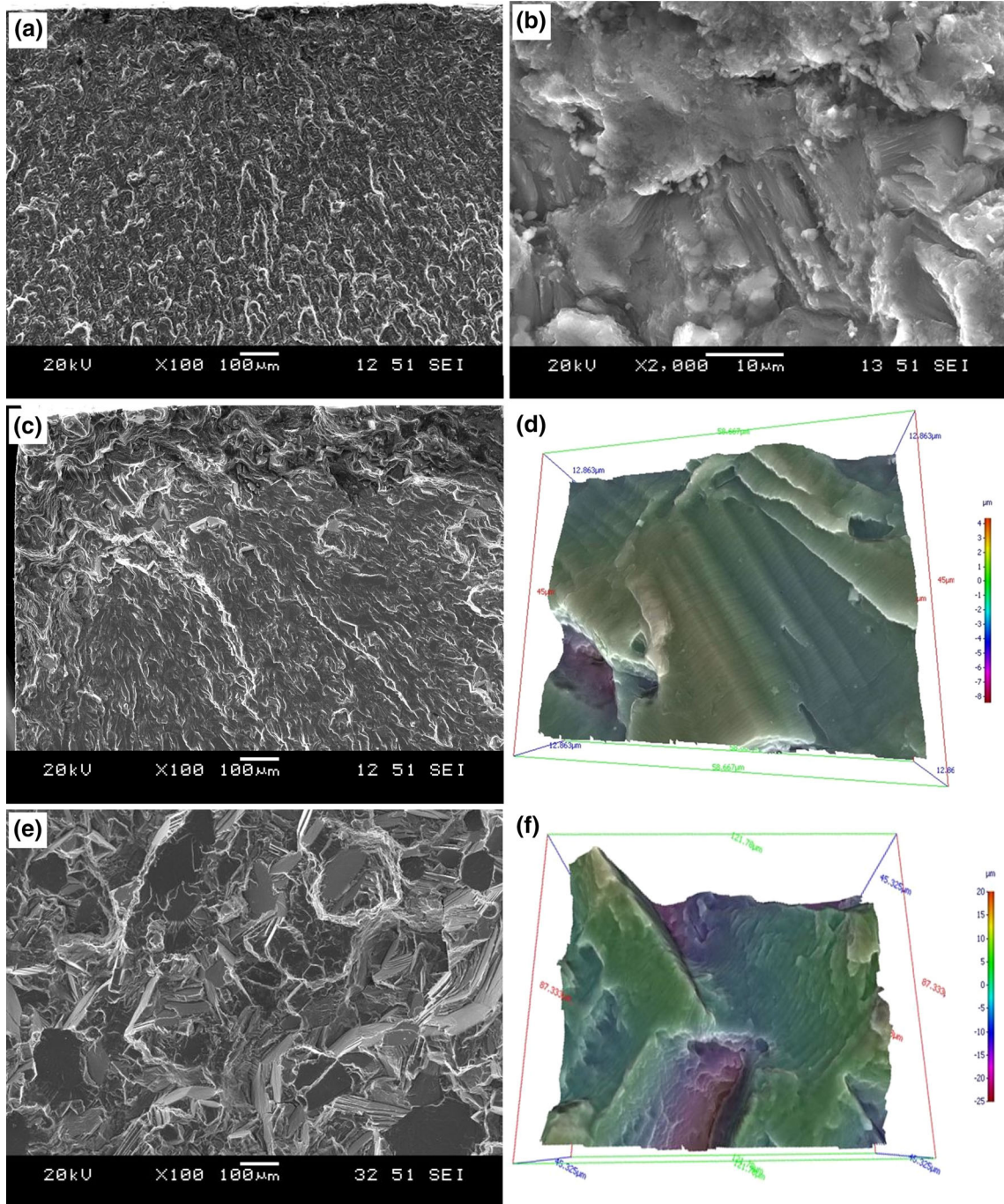


Fig. 13—SEM micrographs of fracture surfaces near crack initiation area (left) and in the propagation zone (right) of the GW103K alloy in the (a) and (b) as-extruded, (c) and (d) T5, and (e) and (f) T6 states fatigued at a strain amplitude of 0.4 pct.

size and small volume fraction of particles might have only small strengthening contributions. Thus, small sized particles or precipitates with an adequate volume fraction would have a significant contribution to the strengthening in RE-Mg alloys, as also reported in Reference 31. As seen from Figure 3(c), a large number of nano-sized dense and uniformly dispersed β' precipitates are obviously the primary strengthening phase of the GW103K alloy in the present T6 condition. It has

also been reported that the β' precipitates, which form on the prismatic planes of α -Mg matrix in a dense triangular arrangement,^[31,59] are perpendicular to the basal plane of α -Mg and very thermally stable at 523 K (250 °C).^[87] Such β' precipitates are particularly effective to impede the movement of dislocations on the basal planes,^[59] thus significantly increase the strength of the Mg alloy in the T6 state as seen from Figure 5 and Table I. It was also reported that the enhanced tensile

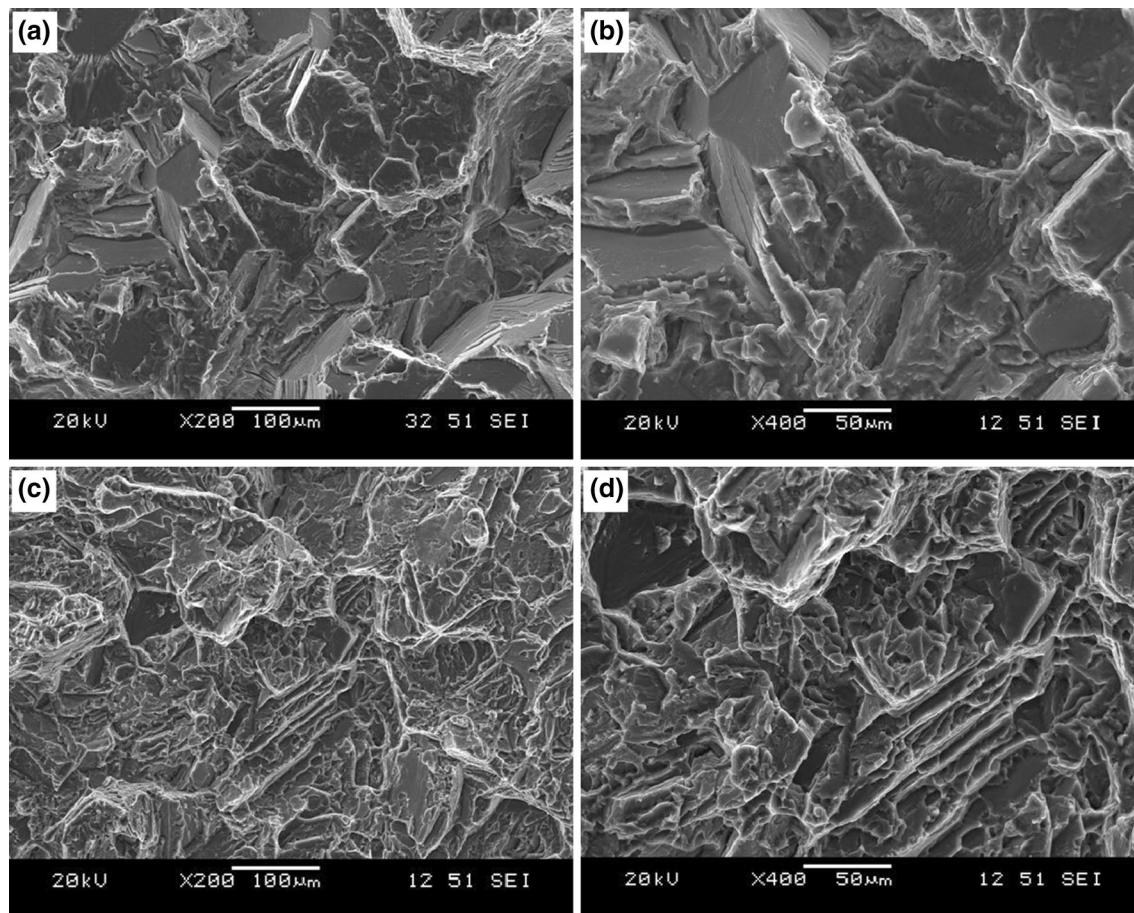


Fig. 14—SEM micrographs of the fracture surface of the T6 sample fatigued at a strain amplitude of 0.4 pct in the region near the upper left corner (*a, b*), and region near the lower right corner (*c, d*) as indicated by the yellow-dashed boxes in Fig. 12(c).

strength in the Mg-6Gd-1Zn-0.6Zr alloy resulted from a uniform and dense distribution of basal precipitate plates.^[31] As mentioned earlier, while the T5 heat treatment may not result in the same level of precipitates in the T6 state due to the lack of solution treatment stage to form a supersaturated solid solution, the smaller grain size shown Figure 1(c) would greatly enhance the strength according to the Hall-Petch relationship,^[70] in comparison with the much larger grain size in the T6 state (Figure 1(e)). As the result, the tensile properties in the T5 state are nearly the same as those in the T6 (Figure 5 and Table I).

B. Effect of Heat Treatment on Cyclic Deformation Characteristics

As compared to the as-extruded GW103K alloy, some obvious improvements in the cyclic deformation resistance have been observed in the T5 and T6 conditions. For example, the maximum and minimum peak stresses in the T5 and T6 conditions were much higher than those in the as-extruded condition in different hysteresis loops as seen from Figure 6. At a given total strain amplitude, the cyclic stress amplitude increased and plastic strain amplitude decreased after the T5 and T6 heat treatment, with a big change from the as-extruded

state to T5 state and a relatively small change from T5 to T6 state (Figures 7 and 8). All of these changes during cyclic deformation corresponded well to those in the monotonic tensile properties (Figure 5 and Table I). To further identify the difference from the RE-free Mg alloys, the stress-strain hysteresis loop of the mid-life cycle for an AM30 extruded alloy is plotted in Figure 15,^[17] along with that of the present RE-containing GW103K alloy in various states. It is seen from Figure 15 that the hysteresis loops of AM30 alloy showed a strong Bauschinger-like effect associated with a skewed asymmetrical shape. While the maximum peak stress of extruded AM30 alloy was close to that of the GW103K alloy in the as-extruded state, the compressive yielding of the AM30 alloy in the descending phase occurred much earlier, giving rise to a much smaller minimum peak stress (absolute value). Similar results were also reported by other investigators.^[11,12,17] The ratio of the compressive-to-tensile peak stress at a total strain amplitude of 1.2 pct was ~0.55 for AM30 alloy, and almost 1 for the GW103K alloy in different states, indicating that the tension-compression asymmetry was no longer existent in the present GW103K, irrespective of alloy states. Typically, the tension-compression yield asymmetry in polycrystalline alloys is directly related to the presence of strong crystallographic texture which

dominates the orientation of slip or twinning planes and directions relative to the externally applied stress.^[88] Yin *et al.*^[89] reported that randomly textured casting samples exhibited almost no yielding asymmetry. Likewise, Patel *et al.*^[78,90] also observed no yielding asymmetry in the super-vacuum die cast or semi-solid processed AM60B and AZ91D Mg alloys, which was in agreement with the results of GW103K alloy. As mentioned earlier in Section III–A, the present GW103K alloy showed relatively weak textures (Figure 4) due to the presence of RE-rich particles and smaller grain sizes (which resulted from the Zener-pinning effect) as compared to the RE-free Mg alloys (Figures 1 and 2). As seen from Figure 16 which shows the distribution of deformation features in the area near the fracture surface in the fatigued samples of AM30 alloy and GW103K alloy in different states, it can clearly be seen that the grain sizes of the RE-Mg alloy were smaller than the RE-free AM30 alloy even after the T6 heat treatment (Figures 16(d) vs (a)), which were partially responsible for the nearly symmetrical hysteresis loops (Figures 6 and 15) via reduced twinning activities. It was reported that grain size had a significant effect on the tendency of twinning because the energy required to form twin interfaces was particularly high in the fine-grained Mg alloy,^[91] and the difference between the tensile and compressive yield strengths generally decreased with decreasing grain size.^[92] More obvious and dense residual twins appeared near the fracture surface area of RE-free AM30 alloy as shown in Figure 16(a),^[17] while twins could barely be visible in the near fracture surface area of the as-extruded GW103K alloy (Figure 16(b)^[17]). Although a few twins could be seen to occur in the grains oriented favorably as the grain sizes increased considerably due to the T6 heat treatment (as indicated by arrows in Figure 16(d)), the number of twins was limited, which was mostly replaced by the fine and uniformly distributed slip lines/bands in the RE-containing GW103K

alloy in all the states (Figures 16(b) through (d)). Such an important change in the deformation mode from predominantly twinning in the RE-free AM30 Mg alloy to mainly dislocation slip in the RE-containing GW103K alloy obviously resulted from (i) the grain refinement (Figure 1), (ii) the uniformly distributed large number density of bamboo-leaf-shaped β' precipitates (Figure 3), and (iii) the texture weakening (Figure 4) in the GW103K alloy, in comparison with AM30 Mg alloy. The combined role of these factors is responsible for the reduction or absence of the hysteresis loop asymmetry (Figures 6 and 14), the increase in the stress amplitude (Figure 7) and the decrease in the plastic strain amplitude at a given total strain amplitude (Figure 8), and eventually the increase in the fatigue life (Figure 9^[17]) via suppressing the twinning activities in the present GW103K alloy, as compared to the RE-free AM30 Mg alloy. The vital role of the RE elements in this regard will be discussed further in the following section.

C. Interaction Between Twins and Precipitates

An important factor that influences the formation of twins in tension–compression cyclic deformation is precipitates. It has been reported that the presence of precipitates in the path of a migrating twin boundary can significantly influence the twinning behavior of an alloy.^[17,88,93] In the present GW103K alloy, the presence of β' precipitates has been confirmed (Figure 3) and it was also reported by Jain *et al.*^[88] that this kind of precipitates can act as the barricade or obstacles which can bring about strengthening by pinning the twinning dislocations and restricting boundary motion. The interaction between twinning and precipitates has been considered to arise primarily from the difficulty experienced by the migrating twin boundaries during the propagation of the twin through densely distributed precipitates.^[88] To better understand the interaction between a twin and plate-shaped precipitates (β' precipitates), which form on the prismatic planes of the matrix in a dense triangular arrangement, a schematic illustration showing the barricade of a precipitate/particle to twinning is plotted in Figure 17. Let us first establish a coordinate system of the hcp unit cell in the Mg matrix with three axes, *i.e.*, a_1 $[2\bar{1}10]$, a_2 $[\bar{1}2\bar{1}0]$, and a_3 $[\bar{1}\bar{1}20]$ which are positioned on the basal $\{0001\}$ plane as indicated by solid red arrows in Figure 17 and all the three axes are oriented at 120 deg angles to one another, with the c -axis $[0001]$ being perpendicular to the basal $\{0001\}$ plane. As reported by He *et al.*,^[59] the stacking type of atoms in β' precipitates observed in the GW103K alloy (Figure 3(c)) is the same as that of the hcp α -Mg matrix. As mentioned earlier in Section III–A, the orientation of β' precipitates has been verified as c -base-centered orthorhombic system.^[31,59,60] Then the precipitates could be plotted in the basal plane of the α -Mg matrix in such a way that the orientation relationship between the β' precipitate and matrix patterns is $[001]_{\beta'} // [0001]_{\alpha}$, and $[100]_{\beta'} // [2\bar{1}\bar{1}0]_{\alpha}$ as reported in Reference 31, 59, 60. In the Mg alloys, $(1\bar{1}02)$ extension twinning is normally activated when a compressive

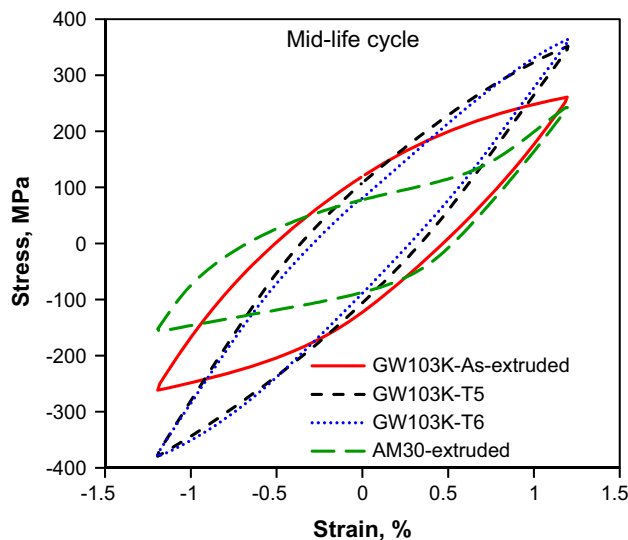


Fig. 15—Typical stress–strain hysteresis loops of the mid-life cycle at a given total strain amplitude of 1.2 pct and strain ratio of $R_e = -1$ for the extruded AM30 and GW103K alloy in different states, respectively.^[17]

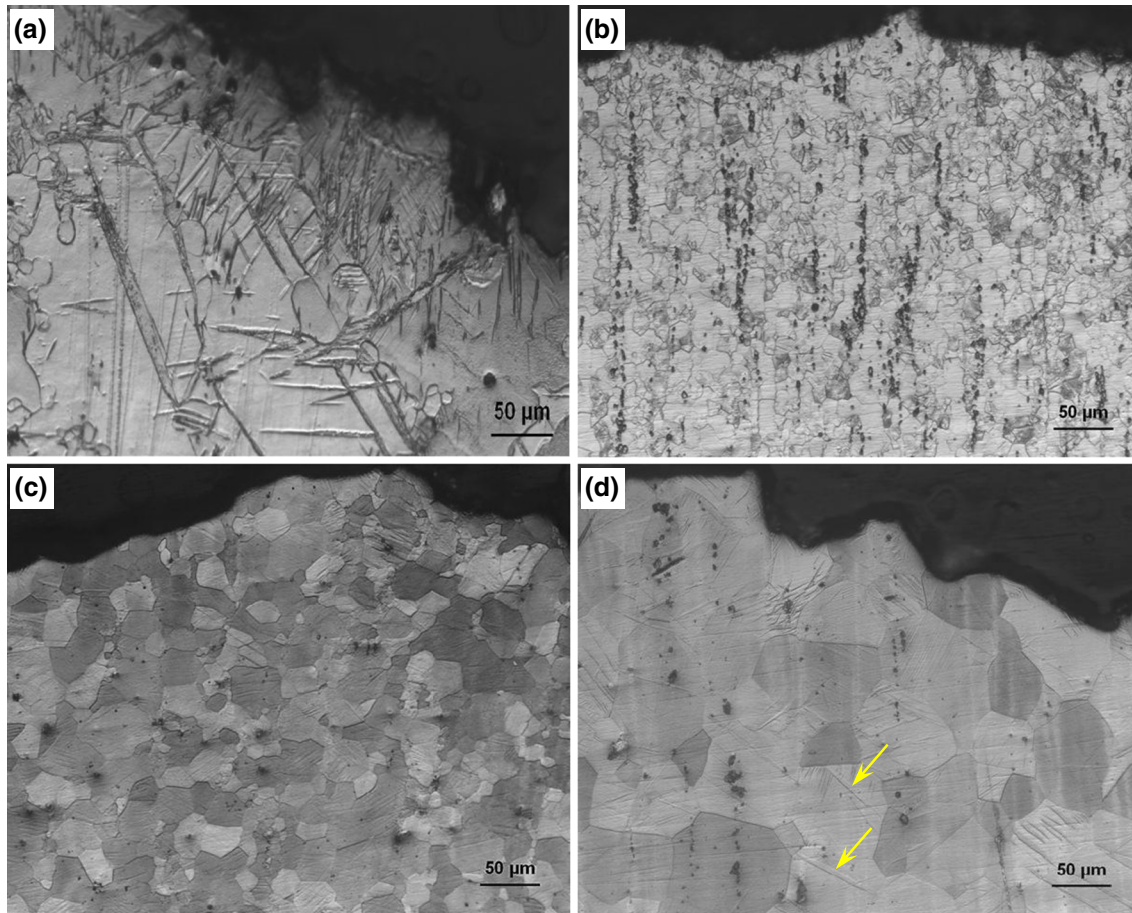


Fig. 16—Optical micrographs in the area near the fracture surface at a strain amplitude of 1.2 pct, showing the distribution of deformation features in the fatigued samples of (a) AM30 alloy,^[17] (b) as-extruded,^[17] (c) T5, and (d) T6 states of the GW103K alloy, respectively.

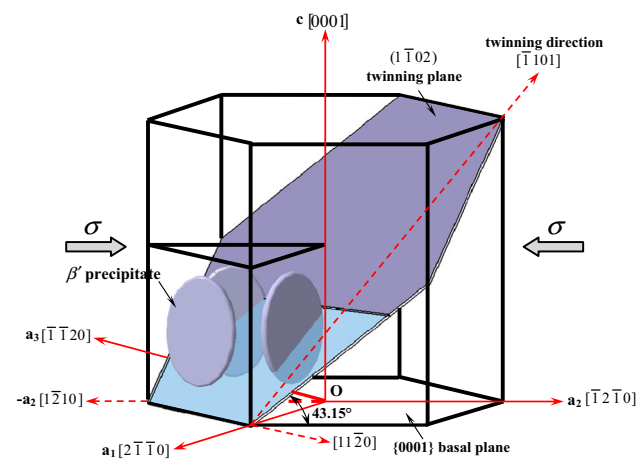


Fig. 17—A schematic illustration of the interaction between $(1\bar{1}02)$ twin and β' precipitate with an orientation relationship of $[100]_{\beta'} // [2\bar{1}\bar{1}0]_{\alpha}$ and $[001]_{\beta'} // [0001]_{\alpha}$ in the GW103K alloy.

stress is applied perpendicular to the $[0001]$ c -axis or parallel to the basal $\{0001\}$ plane.^[76,94] The $(1\bar{1}02)$ extension twinning plane is shown as a shaded color plate and the twinning direction $[\bar{1}\bar{1}01]$ is pointed using a dashed red arrow. Using the Mg lattice parameters of $a = 0.32$ nm and $c = 0.52$ nm,^[95] one can readily

calculate the angle between the basal $\{0001\}$ plane and the $(1\bar{1}02)$ twinning plane to be 43.15 deg, as indicated in Figure 17. If the particle/precipitate cannot be sheared during twinning, as the twinning ledge approaches the precipitate there exists a back stress arising from the harder and more rigid precipitate, which would hinder the free shear of the moving twin ledge and must be overcome by the increasing stress applied.^[17,76,93] In Figure 17, the untwinned portion of the matrix in the absence of twinning due to the blockage of the triangular β' precipitates is indicated by the transparent cyan color in the twinning plane. Furthermore, when the twinning shear reaches the interface between the matrix and the β' precipitate, the movement of atoms towards the precipitate should be accommodated by the basal slip of the matrix near the precipitate/matrix interface.^[17,93] It should also be noted that, the basal slip in the matrix would also be impeded by the β' precipitate, thereby providing an opportunity for the shear to be accommodated by basal slip inside the $(1\bar{1}02)$ twin instead of the parent matrix. Then the need for the additional basal slip on a local scale around the precipitate is likely to increase the stress required to form the twin.^[17,93] It should be pointed out that the schematic diagram in Figure 17, which was not drawn to scale since the precipitates were larger than the hcp unit cell of α -Mg matrix, illustrates only a trio of β'

precipitates in a given grain, so that partial twinning in the grain would be possible. As seen from Figure 3(c) with a magnification of 30,000 \times , a large number of uniformly dispersed triangular groups of plate-shaped β' precipitates are present in a given grain in the present GW103K alloy, thus, the resistance to the formation of twins in the GW103K alloy would be expected to be so huge that almost no twinning would be possible and the dislocation slip became a predominant deformation mode as corroborated from the slip lines shown in Figure 16. The occasionally appeared twins in a very limited number of favorably oriented grains as indicated in Figure 16(d) was attributed to the considerably (\sim 4 times) larger grain size stemming from the solution treatment at 773 K (500 $^{\circ}$ C) for 2 hours.

The above results and analyses indicate that both the grain refinement and the presence of RE-rich precipitates in the present GW103K alloy play a decisive role in suppressing the occurrence of deformation twins, which led to the reduction or elimination of the tension–compression asymmetry (Figures 6 and 15) and the resulting increase of fatigue life (Figure 9^[17]). In short, the addition of RE elements was able to influence substantially the overall cyclic deformation behavior of the GW103K alloy (no matter in which states: as-extruded condition or heat-treated conditions) *via* the refinement of grains, the presence of RE-containing precipitates, the relatively weaker crystallographic texture, and the suppression of twinning activities.

V. CONCLUSIONS

Strain-controlled low-cycle fatigue tests were conducted on a RE containing GW103K alloy in the as-extruded, T5 and T6 conditions under varying strain amplitudes. The following conclusions can be drawn from this investigation:

1. The grain size of the as-extruded GW103K alloy was fairly small (about 12 μ m) in comparison with the RE-free extruded Mg alloys. The average grain size increased to about 25 μ m after T5 peak-aging at 498 K (225 $^{\circ}$ C) for 16 hours. More obvious grain growth (about 92 μ m, being almost four times larger than that after T5 treatment) was observed in the T6 state mainly due to the solution treatment at 773 K (500 $^{\circ}$ C) for 2 hours followed by the peak-aging at 498 K (225 $^{\circ}$ C) for 16 hours.
2. RE-containing particles were present in the GW103K alloy in all the three conditions. After T6 heat treatment, the RE-containing particles contained more Zr and had a more rounded shape. In particular, a high density of nano-sized and bamboo-leaf/plate-shaped β' ($\text{Mg}_7(\text{Gd}, \text{Y})$) precipitates were observed to distribute uniformly in the α -Mg matrix.
3. Unlike the RE-free extruded Mg alloys, the present GW103K alloy in different conditions exhibited basically symmetrical hysteresis loops in tension and compression, suggesting the lack of the tensile-compressive yield asymmetry. This was predominantly attributed to (i) the grain refinement, (ii) the

uniformly distributed large number of bamboo-leaf-shaped β' precipitates, and (iii) the weaker texture.

4. The as-extruded GW103K alloy exhibited cyclic stabilization until failure up to a strain amplitude of 1.0 pct. In the T5 and T6 states, cyclic stabilization occurred up to a strain amplitude of 0.6 pct followed by the slightly cyclic hardening from the strain amplitude of 0.8 to 1.2 pct. Similar to the yield strength and ultimate tensile strength, the maximum and minimum peak stresses in the T5 and T6 conditions were much higher than that in the as-extruded condition.
5. The fatigue life of the GW103K alloy in different states was equivalent within the experimental scatter, which was longer than that of the RE-free extruded Mg alloys, and could be well described by the Coffin–Manson law and Basquin's equation.
6. SEM examinations revealed that fatigue cracks initiated from the specimen surface or near-surface defects in all the three alloy states, and the initiation site contained some cleavage-like facets after T6 heat treatment. Crack propagation was characterized mainly by the typical fatigue striations.

ACKNOWLEDGMENTS

The authors would like to thank the Natural Sciences and Engineering Research Council of Canada (NSERC) and AUTO21 Network of Centres of Excellence for providing financial support. The authors also thank Dr. A.A. Luo from Ohio State University (formerly with General Motors Research and Development Center) for the supply of extruded AM30 magnesium alloy. One of the authors (D.L. Chen) is grateful for the financial support by the Premier's Research Excellence Award (PREA), NSERC-Discovery Accelerator Supplement (DAS) Award, Canada Foundation for Innovation (CFI), and Ryerson Research Chair (RRC) program. X.Q. Zeng would like to thank the Ministry of Science and Technology of China (MOST) and Natural Science Foundation of China (NSFC) for the financial support (Project Nos. 2011BAE22B02, 2011DFA50907, 51171113). The authors would like to thank Dr. R. Tandon and Dr. B. Davies (Magnesium Elektron) for supplying magnesium powders for the defocusing calibration. The authors would also like to thank Messrs. A. Machin, Q. Li, J. Amankrah, and R. Churaman for easy access to the laboratory facilities of Ryerson University and their assistance in the experiments.

REFERENCES

1. T.M. Pollock: *Science*, 2010, vol. 328, pp. 986–87.
2. J.F. Nie, Y.M. Zhu, J.Z. Liu, and X.Y. Fang: *Science*, 2013, vol. 340, pp. 957–60.
3. J. Murray and D. King: *Nature*, 2012, vol. 481 (7382), pp. 433–35.
4. M. McNutt: *Science*, 2014, vol. 345, p. 1429.
5. D. Tittle: *Science*, 2014, vol. 345, p. 361.

6. S.S. Myers, A. Zanobetti, I. Kloog, P. Huybers, A.D.B. Leakey, A.J. Bloom, E. Carlisle, L.H. Dietterich, G. Fitzgerald, T. Hasegawa, N.M. Holbrook, R.L. Nelson, M.J. Ottman, V. Raboy, H. Sakai, K.A. Sartor, J. Schwartz, S. Seneweera, M. Tausz, and Y. Usui: *Nature*, 2014, vol. 510, pp. 139–42.
7. K.U. Kainer: *Magnesium: Alloys and Technology*, Wiley-VCH, Cambridge, 2003.
8. X.B. Liu, R.S. Chen, and E.H. Han: *J. Alloys Compd.*, 2008, vol. 465, pp. 232–38.
9. X.Z. Lin and D.L. Chen: *J. Mater. Eng. Perform.*, 2008, vol. 17 (6), pp. 894–901.
10. X.Z. Lin and D.L. Chen: *Mater. Sci. Eng. A*, 2008, vol. 496, pp. 106–13.
11. S. Begum, D.L. Chen, S. Xu, and A.A. Luo: *Metall. Mater. Trans. A*, 2008, vol. 39A, pp. 3014–26.
12. S. Begum, D.L. Chen, S. Xu, and A.A. Luo: *Int. J. Fatigue*, 2009, vol. 31, pp. 726–35.
13. S. Begum, D.L. Chen, S. Xu, and A.A. Luo: *Mater. Sci. Eng. A*, 2009, vol. 517, pp. 334–43.
14. C.L. Fan, D.L. Chen, and A.A. Luo: *Mater. Sci. Eng. A*, 2009, vol. 519, pp. 38–45.
15. F. Yang, F. Lv, X.M. Yang, S.X. Li, Z.F. Zhang, and Q.D. Wang: *Mater. Sci. Eng. A*, 2011, vol. 528, pp. 2231–38.
16. F.A. Mirza, D.L. Chen, D.J. Li, and X.Q. Zeng: *Mater. Des.*, 2013, vol. 46, pp. 411–18.
17. F.A. Mirza, D.L. Chen, D.J. Li, and X.Q. Zeng: *Mater. Sci. Eng. A*, 2013, vol. 575, pp. 65–73.
18. J.D. Robson, A.M. Twier, G.W. Lorimer, and P. Rogers: *Mater. Sci. Eng. A*, 2011, vol. 528, pp. 7247–56.
19. T. Al-Samman: *Mater. Sci. Eng. A*, 2013, vol. 560, pp. 561–66.
20. X. Li, T. Al-Samman, S. Mu, and G. Gottstein: *Mater. Sci. Eng. A*, 2011, vol. 528, pp. 7915–25.
21. J. Bohlen, S.B. Yi, D. Letzig, and K.U. Kainer: *Mater. Sci. Eng. A*, 2010, vol. 527, pp. 7092–98.
22. R. Cottam, J.D. Robson, G.W. Lorimer, and B. Davis: *Mater. Sci. Eng. A*, 2008, vol. 485, pp. 375–82.
23. J.P. Hadorn, K. Hantzsche, S.B. Yi, J. Bohlen, D. Letzig, and S.R. Agnew: *Metall. Mater. Trans. A*, 2012, vol. 43A, pp. 1363–75.
24. F.A. Mirza, D.L. Chen, D.J. Li, and X.Q. Zeng: *Mater. Sci. Eng. A*, 2013, vol. 588, pp. 250–59.
25. F.A. Mirza, D.L. Chen, D.J. Li, and X.Q. Zeng: *J. Rare Earths*, 2013, in Press.
26. J.P. Hadorn, K. Hantzsche, S.B. Yi, J. Bohlen, D. Letzig, J.A. Wollmershauser, and S.R. Agnew: *Metall. Mater. Trans. A*, 2012, vol. 43A, pp. 1347–62.
27. J.D. Robson: *Metall. Mater. Trans. A*, 2013, vol. 45A, pp. 3205–12.
28. J. Li, R.K. Mishra, and A.K. Sachdev: *Metall. Mater. Trans. A*, 2012, vol. 43A, pp. 2148–57.
29. P. Hidalgo-Manrique, S.B. Yi, J. Bohlen, D. Letzig, and M.T. Pérez-Prado: *Metall. Mater. Trans. A*, 2013, vol. 44A, pp. 4819–29.
30. J.P. Hadorn, R.P. Mulay, K. Hantzsche, S.B. Yi, J. Bohlen, D. Letzig, and S.R. Agnew: *Metall. Mater. Trans. A*, 2013, vol. 44A, pp. 1566–76.
31. S.M. He, X.Q. Zeng, L.M. Peng, X. Gao, J.F. Nie, and W.J. Ding: *J. Alloys Compd.*, 2007, vol. 427, pp. 316–23.
32. F.H. Wang, J. Dong, Y.Y. Jiang, and W.J. Ding: *Mater. Sci. Eng. A*, 2013, vol. 561, pp. 403–10.
33. J. Hirsch and T. Al-Samman: *Acta Mater.*, 2013, vol. 61, pp. 818–43.
34. J. Bohlen, M.R. Nurnberg, J.W. Senn, D. Letzig, and S.R. Agnew: *Acta Mater.*, 2007, vol. 55, pp. 2101–12.
35. J. Dong, W.C. Liu, X. Song, P. Zhang, W.J. Ding, and A.M. Korsunsky: *Mater. Sci. Eng. A*, 2010, vol. 725, pp. 6053–63.
36. Y. Yang, Y.B. Liu, S.Y. Qin, and Y. Fang: *J. Rare Earths*, 2006, vol. 24, pp. 591–95.
37. Y. Yang and Y.B. Liu: *Mater. Charact.*, 2008, vol. 59, pp. 567–70.
38. H. Bayani and E. Saebnoori: *J. Rare Earths*, 2009, vol. 27, pp. 255–58.
39. L. Nascimento, S.B. Yi, J. Bohlen, L. Fuskova, D. Letzig, and K.U. Kainer: *Proc. Eng.*, 2010, vol. 2, pp. 743–50.
40. Y.L. Xu, K. Zhang, X.G. Li, J. Lei, Y.S. Yang, and T.J. Luo: *Trans. Nonferrous Met. Soc. China*, 2008, vol. 18, pp. 306–11.
41. M. Mokhtarishirazabad, S.M.A. Boutorabi, M. Azadi, and M. Nikravan: *Mater. Sci. Eng. A*, 2013, vol. 587, pp. 179–84.
42. L. Wu, Z. Yang, W. Xia, Z. Chen, and L. Yang: *Mater. Des.*, 2012, vol. 36, pp. 47–53.
43. C.Y. Ma, X. Che, B. Zhao, and L.J. Chen: *J. Northeast. Univ.*, 2007, vol. 28, pp. 144–49.
44. M. Mokhtarishirazabad, M. Azadi, G.H. Farrahi, G. Winter, and W. Eichlseder: *Mater. Sci. Eng. A*, 2013, vol. 588, pp. 357–65.
45. X. Song, W.C. Liu, J.P. Belnoue, J. Dong, G.H. Wu, W.J. Ding, S.A.J. Kimber, T. Buslaps, A.J.G. Lunt, and A.M. Korsunsky: *Int. J. Fatigue*, 2012, vol. 42, pp. 284–95.
46. S.M. Yin and S.X. Li: *J. Mater. Sci. Technol.*, 2013, vol. 29 (8), pp. 775–80.
47. R. Zhu, X.T. Cai, Y.J. Wu, L.G. Liu, W.Q. Ji, and B. Hua: *Mater. Des.*, 2014, vol. 53, pp. 992–97.
48. Z.-K. Peng, X.-M. Zhang, J.-M. Chen, Y. Xiao, and H. Jiang: *Mater. Sci. Technol.*, 2005, vol. 21, pp. 722–26.
49. F. Zhang, K.X. Zhang, C.W. Tan, X.D. Yu, H.L. Ma, F.C. Wang, and H.N. Cai: *Trans. Nonferrous Met. Soc. China*, 2011, vol. 21, pp. 2140–46.
50. W. Liu, G. Wu, C. Zhai, W. Ding, and A.M. Korsunsky: *Int. J. Plast.*, 2013, vol. 49, pp. 16–35.
51. L. Wang, Q.Y. Qin, C.W. Tan, F. Zhang, and S.K. Li: *Proc. SEM Annu. Conf.*, Indianapolis, IN, 2010.
52. W.C. Liu, J. Dong, X. Song, J.P. Belnoue, F. Hofmann, W.J. Ding, and A.M. Korsunsky: *Mater. Sci. Eng. A*, 2011, vol. 528, pp. 2250–58.
53. N. Hort, Y. Huang, D. Fechner, M. Stormer, C. Blawert, F. Witte, C. Vogt, H. Drucker, R. Willumeit, K.U. Kainer, and F. Feyerabend: *Acta Biomater.*, 2010, vol. 6, pp. 1714–25.
54. H. Okamoto: *J. Phase Equilib. Diffus.*, 2010, vol. 31(2), p. 199.
55. R. Arroyave, D. Shin, and Z.K. Liu: *Comput. Coupling Phase Diagr. Thermochem.*, 2005, vol. 29, pp. 230–38.
56. S. Khawaled, M. Bamberger, and A. Katsman: in *Magnesium Technology*, S.N. Mathaudhu, W.H. Sillekens, N.R. Neelameggham, and N. Hort, eds., TMS (The Minerals, Metals and Materials Society), John Wiley & Sons, Inc., Hoboken, NJ, 2012.
57. Z.J. Liu, G.H. Wu, W.C. Liu, S. Pang, and W.J. Ding: *Trans. Nonferrous Met. Soc. China*, 2012, vol. 22, pp. 1540–48.
58. Z.H. Wang, W.B. Du, X.D. Wang, K. Liu, and S.B. Li: *Trans. Nonferrous Met. Soc. China*, 2013, vol. 23, pp. 593–98.
59. S.M. He, X.Q. Zeng, L.M. Peng, X. Gao, J.F. Nie, and W.J. Ding: *J. Alloys Compd.*, 2006, vol. 421, pp. 309–13.
60. X. Gao, S.M. He, X.Q. Zeng, L.M. Peng, W.J. Ding, and J.F. Nie: *Mater. Sci. Eng. A*, 2006, vol. 431, pp. 322–27.
61. L. Gao, J. Zhou, Z.M. Sun, R.S. Chen, and E.H. Han: *Chin. Sci. Bull.*, 2011, vol. 56 (11), pp. 1142–46.
62. M. Nishijima, K. Hiraga, M. Yamasaki, and Y. Kawamura: *Mater. Trans.*, 2006, vol. 47 (8), pp. 2109–12.
63. F. Lv, F. Yang, Q.Q. Duan, Y.S. Yang, S.D. Wu, S.X. Li, and Z.F. Zhang: *Int. J. Fatigue*, 2011, vol. 33, pp. 672–82.
64. N. Stanford and M.R. Barnett: *Scripta Mater.*, 2008, vol. 58, pp. 179–82.
65. N. Stanford, D. Atwell, and M.R. Barnett: *Acta Mater.*, 2010, vol. 58, pp. 6773–83.
66. S.R. Agnew, M.H. Yoo, and C.N. Tome: *Acta Mater.*, 2001, vol. 49, pp. 4277–89.
67. L.W.F. Mackenzie and M.O. Pekguleryuz: *Scripta Mater.*, 2008, vol. 59, pp. 665–68.
68. M.T. Perez-Prado and O.A. Ruano: *Scripta Mater.*, 2002, vol. 46, pp. 149–55.
69. W.G. Yang and C.H. Koo: *Mater. Trans.*, 2003, vol. 44, pp. 1029–35.
70. G.E. Dieter: *Mechanical Metallurgy, SI Metric Edition*, McGraw-Hill Inc., New York, NY, 1986.
71. S. Suresh: *Fatigue of Materials*, 2nd ed., Cambridge University Press, Cambridge, 1998.
72. C.H. Cáceres, T. Sumitomo, and M. Veidt: *Acta Mater.*, 2003, vol. 51 (20), pp. 6211–18.
73. Q. Yu, J. Zhang, Y. Jiang, and Q. Li: *Int. J. Fatigue*, 2012, vol. 36, pp. 47–58.
74. J.B. Jordon, J.B. Gibson, M.F. Horstemeyer, H. El-Kadiri, J.C. Baird, and A.A. Luo: *Mater. Sci. Eng. A*, 2011, vol. 528, pp. 6860–71.

75. T.J. Luo, Y.S. Yang, W.H. Tong, Q.Q. Duan, and X.G. Dong: *Mater. Des.*, 2010, vol. 31, pp. 1617–21.
76. F.A. Mirza and D.L. Chen: in *Aerospace Materials Handbook*, S. Zhang and D.L. Zhao, eds., CRC Press, New York, 2013, pp. 647–698.
77. S.H. Chowdhury, D.L. Chen, S.D. Bhole, E. Powidajko, D.C. Weckman, and Y. Zhou: *Metall. Mater. Trans. A*, 2012, vol. 43A, pp. 2133–47.
78. H.A. Patel, D.L. Chen, S.D. Bhole, and K. Sadayappan: *Mater. Des.*, 2013, vol. 49, pp. 456–64.
79. S.Q. Wang, J.H. Liu, and D.L. Chen: *Mater. Des.*, 2013, vol. 49, pp. 716–27.
80. S.H. Chowdhury, D.L. Chen, S.D. Bhole, X. Cao, and P. Wanjara: *Mater. Sci. Eng. A*, 2013, vol. 562, pp. 53–60.
81. S.M. Chowdhury, D.L. Chen, S.D. Bhole, E. Powidajko, D.C. Weckman, and Y. Zhou: *Metall. Mater. Trans. A*, 2011, vol. 42A, pp. 1974–89.
82. B.S. Naik, D.L. Chen, X. Cao, and P. Wanjara: *Metall. Mater. Trans. A*, 2013, vol. 44A, pp. 3732–46.
83. C. Laird: *Fatigue Crack Propagation*, ASTM STP 415, ASTM International, West Conshohocken, PA, 1967.
84. A. Beaber and W. Gerberich: *Nat. Mater.*, 2010, vol. 9, pp. 698–99.
85. Q.M. Peng, X.L. Hou, L.D. Wang, Y.M. Wu, Z.Y. Cao, and L.M. Wang: *Mater. Des.*, 2009, vol. 30, pp. 292–96.
86. M. Matsuda, S. Ando, and M. Nishida: *Mater. Trans.*, 2005, vol. 46, pp. 361–64.
87. D.D. Yin, Q.D. Wang, Y. Gao, C.J. Chen, and J. Zheng: *J. Alloys Compd.*, 2011, vol. 509, pp. 1696–1704.
88. J. Jain, W.J. Poole, C.W. Sinclair, and M.A. Gharghour: *Scripta Mater.*, 2010, vol. 62, pp. 301–04.
89. S.M. Yin, C.H. Wang, Y.D. Diao, S.D. Wu, and S.X. Li: *J. Mater. Sci. Technol.*, 2011, vol. 27, pp. 29–34.
90. H.A. Patel, N. Rashidi, D.L. Chen, S.D. Bhole, and A.A. Luo: *Mater. Sci. Eng. A*, 2012, vol. 546, pp. 72–81.
91. J. Koike, T. Kobayashi, T. Mukai, H. Watanabe, M. Suzuki, K. Maruyama, and K. Higashi: *Acta Mater.*, 2003, vol. 51, pp. 2055–65.
92. J. Bohlen, P. Dobron, J. Swiostek, D. Letzig, F. Chmelik, P. Lukac, and K.U. Kainer: *Mater. Sci. Eng. A*, 2007, vol. 462, pp. 302–06.
93. N. Stanford and M.R. Barnett: *Mater. Sci. Eng. A*, 2009, vol. 516, pp. 226–34.
94. Y.N. Wang and J.C. Huang: *Acta Mater.*, 2007, vol. 55, pp. 897–905.
95. P.G. Partridge: *Int. Mater. Rev.*, 1967, vol. 12, pp. 169–94.